FACULDADE DE ENGENHARIA DA UNIVERSIDADE DO PORTO


# Biocomputational model for urodynamic analysis

**João Pedro Vendas dos Santos**

Mestrado Integrado em Engenharia Mecânica

Supervisors:
Prof. Dr. Renato Natal
Prof. Dr. Marco Parente
Dr. Dulce Oliveira

July 19, 2018

# Biocomputational model for urodynamic analysis

**João Pedro Vendas dos Santos**

Mestrado Integrado em Engenharia Mecânica

July 19, 2018

# Abstract

Urinary incontinence (UI) affects millions of people worldwide, harming their emotional, psychological and social life. Urodynamics has been a crucial tool to assess the functioning of the lower urinary tract and to determine the best possible treatment for UI. However, the outcome of these tests depends, partially, on the patient's psychological state, which undoubtedly influences it.

It is unquestionable that computational modeling could aid better understanding of the coordinated performance of the bladder and urethra during micturition cycle. It has been a crucial tool regarding the advances in different areas of science, especially in biomechanics.

The purpose of this work is to obtain a biocomputational model to accurately model a lower urinary tract dysfunction and to identify and compare the mechanical changes that lead to the problem. To do so, a model of the bladder and urethra, based on magnetic resonance imaging data of a nulliparous female without pelvic floor dysfunction complaints, was used. To characterize the bladder tissue behavior, experimental tests from the literature were reproduced using different constitutive models. A thorough focus on the mechanical properties to characterize its typical mechanical behavior (large deformations with slight pressure variations) was taken. Then, computational analysis with fluid-structure interaction was performed, simulating the bladder's filling. Lastly, to calibrate the computational model, experimental data from urodynamics was used.

As far as isotropic hyperelastic constitutive models are concerned, the Yeoh and Ogden models showed to mimic the bladder's wall behavior in an extremely satisfactory way. The conducted simulations regarding the bladder's filling suggested that both stress urinary incontinence and overactive bladder patients exhibit a stiffer bladder's wall. They also suggested that a more complex constitutive model, such as Martins's model, should be used in order to obtain rigorous results, since in this way it is possible to mimic muscle contractions which are crucial to represent data from urodynamics.

# Resumo

A incontinência urinária afeta milhões de pessoas em todo o mundo, afetando a sua vida emocional e social. Os exames urodinâmicos têm sido uma ferramenta fundamental para avaliar o funcionamento do trato urinário inferior e para identificar o tratamento adequado para o tipo de incontinência urinária detetada. Porém, o resultado destes exames depende, parcialmente, do estado psicológico do paciente que, sem dúvida, os influencia.

É inquestionável que a modelação computacional possa contribuir para uma melhor perceção do funcionamento coordenado da bexiga e da uretra durante o ciclo de micção. Esta tem sido fundamental para os avanços que se têm verificados nas diferentes áreas da ciência, especialmente na biomecânica.

O objetivo desta tese é obter um modelo biocomputacional para modelar uma disfunção existente no trato urinário inferior e identificar e comparar as alterações mecânicas que conduziram ao problema. Assim, foi usado um modelo constituido pela bexiga e uretra, resultante de imagens provenientes de ressonânia magnética de uma mulher sem filhos e sem qualquer tipo de disfunção na cavidade pélvica. No sentido de caracterizar o comportamento da parede da bexiga, foram reproduzidos ensaios mecânicos provenientes da literatura, usando diferentes modelos constitutivos. De seguida, uma análise computacional com interação fluido-estrutura foi realizada, simulando desta forma o normal enchimento da bexiga. Finalmente, no sentido de calibrar o modelo, usaram-se dados provenientes de exames urodinâmicos.

Os modelos de Yeoh e Ogden revelaram representar, de forma bastante satisfatória, o comportamento da parede da bexiga. No que diz respeito às simulações realizadas para mimetizar o enchimento deste orgão, estas sugerem que a parede da bexiga é mais rígida, tanto em pacientes que apresentem incontinência urinária de esforço como hiperatividade da bexiga, comparativamente com pacientes que apresentem uma bexiga saudável. Foi possível, ainda, concluir que a utilização de modelos constitutivos mais complexos, como é o caso do modelo de Martins, é essencial para a obtenção de resultados mais rigorosos e realistas, já que este nos permite simular a contração do músculo da parede da bexiga.

# Agradecimentos

Ao Professor Doutor Renato Natal gostaria de agradecer a oportunidade e confiança dadas para a realização deste trabalho.

Ao Professor Doutor Marco Parente agradeço, não só a disponibilidade e apoio prestados, bem como a partilha de conhecimentos que permitiu solucionar alguns obstáculos encontrados.

À Doutora Dulce Oliveira pelo incansável apoio, disponibilidade, partilha de conhecimento e incentivo demonstrados ao longo da realização desta dissertação. Agradeço, igualmente, a sua constante e contagiante boa disposição.

Ao Bruno Areias pela disponibilidade e apoio prestados, bem como pela partilha de conhecimento.

À minha família, em especial à minha tia pelo constante incentivo e aos meus pais pela oportunidade proporcionada para enriquecer o meu conhecimento. Gostaria, ainda, de agradecer à minha mãe pelo incansável e permanente acompanhamento e apoio prestados ao longo desta longa caminhada.

João Santos

*"Life is like riding a bicycle.*
*To keep your balance, you must keep moving"*

Albert Einstein

# Contents

# List of Figures

# List of Tables

# Abbreviations

| | |
|---|---|
| ALPP | Abdominal leak point pressure |
| AUM | Ambulatory urodynamic monitoring |
| DLPP | Detrusor leak point pressure |
| EMG | Electromyography |
| FEM | Finite element method |
| FDV | First desire to void |
| FSF | First sensation of filling |
| ICS | International continence society |
| ISD | Intrinsic sphincter deficiency |
| LUT | Lower urinary tract |
| MCC | Maximum cystometric capacity |
| MRI | Magnetic resonance imaging |
| MUCP | Maximum urethral closure pressure |
| MUP | Maximum urethral pressure |
| OB | Overactive bladder |
| PVR | Post-void residual |
| SDV | Strong desire to void |
| SUI | Stress urinary incontinence |
| UCPP | Urethral closure pressure profile |
| UI | Urinary incontinence |
| UPP | Urethral pressure profile |
| UUT | Upper urinary tract |

# Chapter 1

# Introduction

## 1.1 Context

Urinary incontinence (UI) affects millions of people worldwide, conditioning their emotional, psychological and social life. Many people who suffer from UI think it is a natural cause of aging and believe nothing can be done. They are afraid of doing several activities that were on their daily routine, becoming complacent and preventing them from appreciating life.

Fortunately, nowadays, with urodynamics it is possible to assess the performance of the lower urinary tract, in order to provide objective pathophysiological explanations for symptoms and also for any dysfunction of the lower and upper urinary tract. Besides, indirectly, it also aids choosing an appropriate treatment for the existing incontinence and its associated pathology. Urodynamic studies play a crucial role when it comes to confirming the effects of treatment or to understand the mode of action of a particular type of treatment, especially a new one. Despite being the only available tool to evaluate the performance of the lower urinary tract, urodynamic techniques are invasive. Thus, the outcome of these tests depends on the patient's psychological state.

In order to overcome this and other handicaps of urodynamics, the usage of tools such as computational modeling may be the key to a better understanding of the lower urinary tract dysfunctions and to their treatment. There is no doubt that it has been a decisive tool regarding the progress achieved in numerous fields of science, mainly due to the development of numerical techniques, in particular the Finite Element Method (FEM). Physical phenomena is described by means of mathematics, in particular differential equations which exact solutions most of the times are hard to obtain. With FEM it is possible to achieve approximate solutions even in situations with complex structures and interactions. However, in order to get reliable results it is crucial to understand, not only the geometry and the boundary conditions of what is being analysed, but also its mechanical properties, which in some living tissues are still an obstacle to overcome.

In this regard, continuum mechanics aids in obtaining the necessary constitutive equations to access the stresses and strains experienced by materials. As far as living tissues are concerned, they exhibit a complex behavior. The presence of fibers induces the anisotropy that is characteristic of them. In addition, they have a time-dependent behavior, meaning that their current mechanical

state depends on the previous loading events they were subjected. Gathering all these details in one constitutive model has not been an easy task. However, constitutive models with such complexity already exist.

This work intends to obtain the parameters of the constitutive models available in Abaqus software, as well as to compare them with more complex models - the Martins's model [1] -, in order to mimic the bladder's wall behavior. This, combined with the calibrarion of the bladder's wall behavior with data from urodynamics, characterizing different types of urinary incontinence, will make it possible to compare the mechanical changes in a normal functioning of the bladder with the changes corresponding to different types of urinary incontinence.

## 1.2 Thesis structure

In Chapter 2 an overview regarding the anatomy of the urinary tract is made. Afterwards, the normal behavior of the lower urinary tract is presented, as well as the most common types of urinary incontinence.

Chapter 3 provides information related to the existing urodynamic studies and what can be assessed in each of them. Advantages and disadvantages and the standard procedure are also presented.

Chapter 4 focus on the basis of the constitutive equations used to characterize hyperelastic materials. A thorough analysis of the most common used tensors is made. Some hyperelastic constitutive models are presented, including anisotropic constitutive models. An overview of viscoelasticity and the Finite Element Method is also provided.

In Chapter 5 the simulations that were conducted are presented, providing the accuracy of each constitutive model used as far as mimicking the bladder's wall behavior is concerned.

Finally, in Chapter 6 some final remarks regarding the objectives of this thesis and about possible future work are made.

# Chapter 2

# The Urinary Tract

The human urinary tract is a contiguous hollow organ system. Its primary function is to collect, transport, store and expel urine in a coordinated manner in order to remove waste products from the body. It also regulates water and salt balance.

The urinary tract is comprised of the kidneys, ureters, urinary bladder and the urethra. Each of them has distinct anatomic features and plays crucial functions [2].

The urinary tract can be divided in the upper urinary tract (UUT), embracing the kidneys and ureters, and in the lower urinary tract (LUT), containing the urinary bladder, urethra and, in men, also the prostate [3].

## 2.1 The Upper Urinary Tract

As far as the kidneys are concerned, they are located posterior to the peritoneum (a large membrane in the abdominal cavity that connects and supports internal organs), just below the ribcage. Each kidney is covered in three layers - an inner layer, a middle layer full of adipose tissue and a tough outer layer that protects it from physical damage. Under these layers is the inside of the kidney where blood flows and is filtered through the nephrons resulting in urine generation. The kidneys are supposed to remove waste substances from the blood, create a good balance between water and salt in the body and, finally, to produce hormones [4], [5].

Regarding the ureters, they are fibromuscular tubes with approximately 30 cm long. They connect the kidneys to the bladder, where they enter at an angle which makes it possible to create a valve that prevent the urine to flow back towards the kidneys (reflux). Their wall has three layers, including a muscle layer which helps the ureters to accomplish their function - to convey urine from kidneys to the bladder [5], [6].

## 2.2 The Lower Urinary Tract

As previously stated, the lower urinary tract embraces the urinary bladder, urethra and the prostate, in men. The bladder is a hollow and distensible organ which anatomical position differs, regarding

its degree of distension. When empty, the bladder is an entirely extraperitoneal pelvic organ and lies behind the *symphysis pubis* with the shape of a tetrahedron. On the other hand, when filled, it has an ovoid shape and it rises well above the *symphysis pubis*, becoming an abdominal organ [2], [3].

The apex of the tetrahedron points anteriorly towards the superior edge of the pubic sumphysis. In men, the triangular base faces posteriorly towards the rectum, as in women, the base is united with the anterior vaginal wall and the upper part of the cervix, as it is perceptible in figures 2.1 and 2.2, respectively. The lowest part of the bladder is known as the bladder neck. In men, it lies directly on the prostate, while in women it lies in the anterior vaginal wall [3].

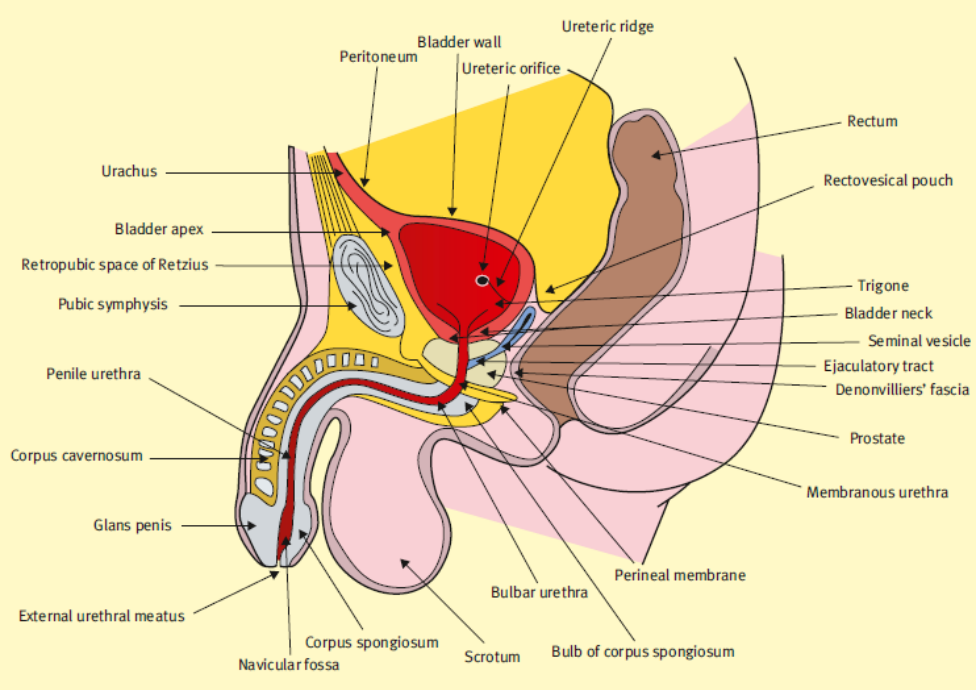


Figure 2.1: Median sagittal section of male pelvis showing the lower urinary tract [3].

The bladder wall, figure 2.3, is a complex structure made of several layers:

- The mucosa - the innermost layer, consists of epithelial cell layers that have the ability to adapt their shape during the filling phase;
- The submucosa - a thick layer of loose connective tissue, rich in elastic fibers, blood, nerve and lymphatic vessels;
- The tunica muscolaris - it has three smooth muscular layers together with connective elements, widely known as the detrusor muscle. In the inner and outer layers of the muscolaris, muscular fibers are predominately distributed from the apex to the bottom of the bladder (longitudinal direction). On the other hand, within the middle layer, the fibers have a circumferential organization;

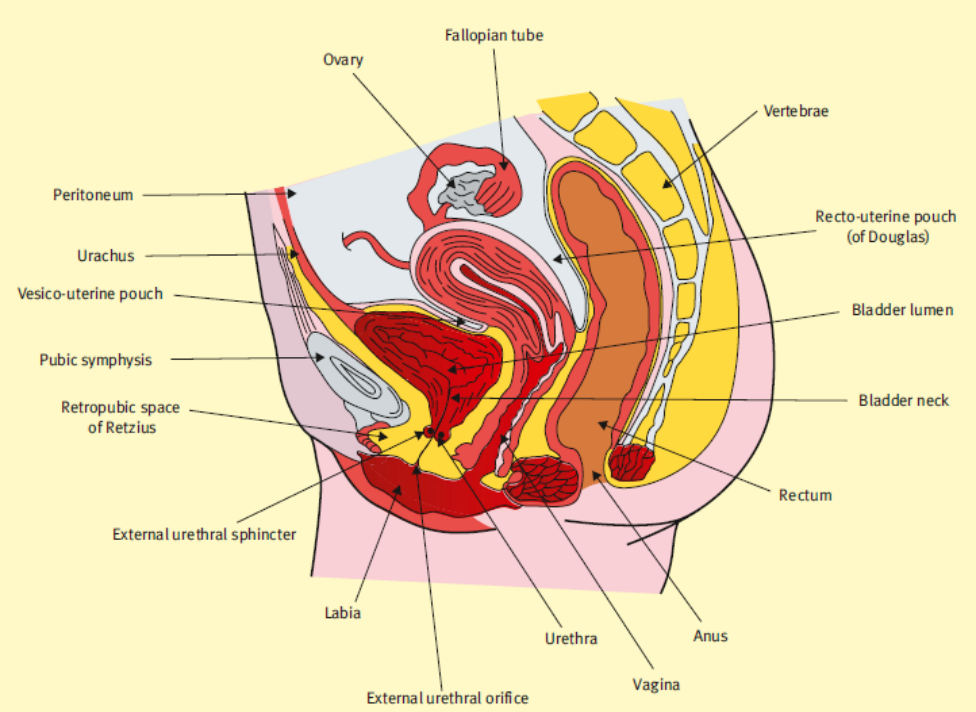


Figure 2.2: Median sagittal section of female pelvis showing the lower urinary tract [3].

- The serosa - it is a visceral peritoneum, which mechanical contribution to the wall stiffness and strength is almost negligible [7].

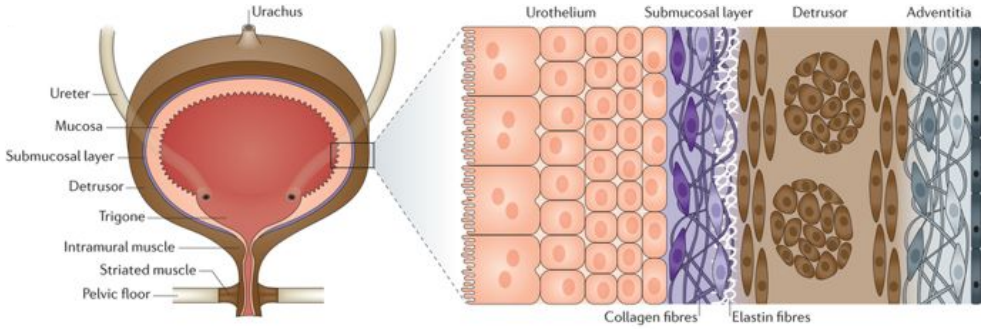


Figure 2.3: Bladder wall layers [8].

The anisotropic and non-linear behavior of the bladder's wall is known to be entailed by its complex configuration, particularly, by its fibrous components. They play a crucial role in the bladder's functions - to storage the urine at low pressure (its capacity in an adult is approximately 500 mL) and to expel the urine under voluntary control at high pressure via the urethra [7].

The urethra, which differs in men and women, is contiguous with the bladder neck and its function is to transport the urine from the bladder to the exterior. In men, its total length is approximately 20 cm and it can be divided in four sections - the short prostatic and membranous sections,

which are from the posterior urethra, and the longer bulbar and penile sections, which are from the anterior urethra [2], [3]. In women, the urethra is much shorter, about 4 cm long and it passes below the pubic symphysis embedded in the anterior vaginal wall.

The flow of urine through the urethra is controlled by the internal and external sphinters. They are responsible for the maintenance of urinary continence. The first surrounds the opening of the bladder to the urethra and is continuous with the detrusor muscle. Its contraction and relaxation are involuntary, since it is composed of smooth muscle. It is controlled through the autonomic nervous system. On the other hand, the latter is made of skeletal muscle, thus its contraction and relaxation are voluntary. It is located at the distal inferior end of the bladder in women and at the level of the membranous urethra in men [9].

## 2.3 Normal Lower Urinary Tract Behavior

In order to provide an efficient function of the lower urinary tract, there are several structures that must act together - the pelvic muscles must sustain the bladder and the urethra, the sphincters must be able to open and close the urethra and, finally, the nerves must control the muscles of the bladder and the pelvic floor [10].

Micturition cycle comprises two stages - the storage and the voiding phases. The first stage is accomplished without sensation, as the bladder is filled with urine in a way that the pressure inside it (intravesical pressure) is low and maintained almost constant, which insures adequate drainage of urine flow from the upper urinary tract. This ability, to gather increasing volumes of urine while maintaining a low intravesical pressure, is associated with the elasticity of the bladder wall and is defined as compliance [10], [11].

As the bladder filling continues, a sensation of the need to void increases, followed by the relaxation of the internal sphincter. However, the voiding phase can be delayed for some time, since it is a controlled action. To promote micturition, coordinated relaxation of the pelvic floor and external sphincter, as well as detrusor contraction, contribute to the efficient emptying of the bladder and the flux of urine through the urethra. Urinary flow can be interrupted by voluntary contraction of the external sphincter and pelvic floor [10], [11].

In a normal micturition cycle no uncomfortable sensation such as urgency, pain or discomfort is perceived and no urinary leakage occurs. If any of these symptoms occurs, it should be monitored, even though it does not necessarily mean that there is some type of incontinence and/or dysfunction.

## 2.4 Urinary Incontinence

Urinary incontinence is defined, by the International Continence Society (ICS), as "the complaint of any involuntary leakage of urine". It affects millions of people worldwide, mainly the elderly and women [12].

Besides being a medical problem, urinary incontinence can also affect people's emotional, psychological and social life. There are many types of urinary incontinence, however the most common are:

- Stress urinary incontinence (SUI) - it is one of the most common types of urinary incontinence. The loss of urine is due to an increase of the intra-abdominal pressure caused, for example, by some type of physical activity. It usually happens when pelvic floor muscles are weakened;
- Urge incontinence - it is characterized by a sudden, intense urge to urinate followed by involuntary loss of urine;
- Mixed incontinence - when both stress and urge urinary incontinence are experienced;
- Overactive bladder (OB) - it is associated with urge and frequency symptoms. Bladder muscles (detrusor) contracts even though the bladder is not completely full [13];

As far as urinary incontinence genesis is concerned, there are numerous causes that can lead to any involuntary loss of urine. Weakened pelvic floor muscles as a result of vaginal childbirth, a disease process, injuries from an accident or a consequence of surgery, may lead to it [14].

Unlike many people believe, incontinence is not a direct consequence of aging. However, changes that occur with it may contribute to incontinence. A good example is the natural enlargement of the prostate in men [14].

Since there are several possible causes for incontinence, a physician should be consulted so as to check if it is not a symptom of another medical problem or to be advised of the correct treatment options. If it is suspected that urinary incontinence is due to any lower urinary tract dysfunction, urodynamics may be a good option to find its cause.

# Chapter 3

# Urodynamic Studies

## 3.1 Urodynamic Studies

In order to accurately model and validate bladder activity under filling and voiding conditions, it is important to understand the dynamics of the lower urinary tract [10]. Urodynamics is the key not only to achieve a reliable model but also to find the cause for any abnormality within the lower urinary tract.

The combined study of urine flow in the bladder, the urinary sphincter, and the urethra is called urodynamics. Urodynamic investigations have been the most definitive tests for evaluating the function of the LUT [15], [16].

Urodynamic studies provide a method for objectively assessing how the bladder and urethral coordinated functions of storing and releasing urine are operating, in order to be able to better understand the occurrence of UI and to assist choosing an effective treatment [17]. There are some basic assumptions that aid urodynamics: the bladder has the ability to store urine with a nearly constant low intravesical pressure; the patient has the ability to suppress micturition at all bladder volumes; the patient has the ability to voluntarily initiate the voiding reflex, including relaxation of the urethra and contraction of the detrusor muscle [16].

These assumptions can be evaluated through the various components of urodynamic testing. They comprise unique tests that can be performed individually or together, depending on the desired information. These tests are generally categorized by the specific bladder function they intend to assess. The components of urodynamic testing that evaluate bladder filling and storage include filling cystometry (single or multichannel) with electromyography. Bladder emptying or voiding is evaluated by uroflowmetry and pressure-flow studies (voiding cystometry). Finally, urethral function can be evaluated by urethral pressure profilometry and leak point pressure [16].

It is imperative that urodynamic testing should be performed and recorded in a standardized fashion to promote a clear communication between the various health care practitioners. The ICS has published several reports with the goal of providing standardized terms and definitions for many of the parameters that are evaluated during these tests.

Table 3.1: Basic study conditions to be documented in scientific communications [16].

| |
|---|
| - Investigator |
| - Circumstances during study |
| - Patient conditions (sedation, medication, position, provocation) |
| - Equipment (type, calibration) |
| - Pressure measurement (reference level, transducer) |
| - Catheter (size, side-holes, type for microtip transducer catheter, number of channels, manufacturer) |
| - Fluid (infusate, rate of infusion, temperature) |
| - Method of leakage detection |

In Table 3.1 is presented the basic study conditions that should be reported in scientific articles dealing with urodynamic aspects of urinary incontinence.

In spite of being available to physicians for some time now, urodynamic testing indications remain controversial. There is currently no accepted list of indications for when to obtain urodynamic testing. When determining whether there is need for testing, several factors must be weighed including the cost of the urodynamic testing, patient history, clinical findings, and whether test findings would change treatment or management [16].

The role of urodynamic studies in clinical practice should be:

- to identify or to rule out factors contributing to the LUT dysfunction and assess their relative importance;
- to obtain information about other aspects of LUT dysfunction;
- to predict the consequences of LUT dysfunction for the upper urinary tract;
- to predict the outcome, including undesirable side effects, of a contemplated treatment;
- to confirm the effects of intervention or understand the mode of action of a particular type of treatment, especially a new one;
- to understand the reasons for failure of previous treatments for urinary incontinence, or for LUT dysfunction in general [16]..

## 3.2 Cystometry

The study of the urinary apparatus dynamics through measures of pressure inside the bladder is called Cystometry. It is an invasive urodynamic test and evaluates the relationship between volume and pressure during the filling and storage phases. The aim of Cystometry is to assess bladder sensation, bladder capacity, detrusor activity, and bladder compliance by continuous measurement of the pressure/volume relationship of the bladder [16], [11], [10].

This study comprises the voiding and gradual filling by instilling a filling medium (usually with a filling rate of 50 mL/min), while simultaneously measuring various pressures (abdominal,

vesical, and/or urethral) in order to evaluate the function of the bladder during the filling/storage phase [16], [11], [10].

In spite of, historically, both liquid and gas had been used as the filling medium, gas cystometry is not recommended. Although gas cystometry is quicker and more hygienic in case of incontinence, a physiologic liquid medium is preferable, since gas is unphysiologic and compressible, and easily provokes detrusor overactivity, thus not reliable. The liquid filling medium used may be physiologic saline, water or radiographic contrast. It is important to be aware that its physical properties, its acidity, the type of contrast medium and the concentration of ions such as $K^+$ and $Ca^{2+}$ may affect detrusor overactivity [16], [11], [10].

Several variations of filling cystometry are available, including simple cystometry, single-channel, or multichannel cystometry. The first involves the placement of a catheter that is attached to a 60 cc syringe with the plunger removed placed above the level of the pubic symphysis. Fluid is infused by gravity, with the need to elevate the syringe to maintain filling as bladder pressure increases. Finally, a cough stress test and evaluation of post-void residual (PVR) can be performed at the conclusion of simple cystometry. Because a pressure catheter is not utilized, evaluation of filling pressures cannot be assessed. However, evaluation of bladder sensation and the determination of detrusor contractions can be obtained using this simple test. If more information is desired, filling cystometry can be performed using a single catheter in the bladder (single-channel cystometry) or multiple catheters (multichannel cystometry) [16], [11], [10].

Single-channel cystometry allows measuring vesical pressure, but does not account for the pressure-related events from abdominal strain or patients' activity. It is not capable of informing if a rise in bladder pressure is due to a bladder contraction or to an increase in intra-abdominal pressure transmitted to the bladder, since the measured intravesical pressure is the sum of the pressure caused by bladder wall events (detrusor contraction) and the pressure caused by extravesical sources (abdominal straining). These factors can only be captured if abdominal pressure measurement is added, as recorded in multichannel cystometry. Therefore, it is performed routinely over single-channel cystometry [16], [11], [10].

In multichannel cystometry two catheters are placed to measure vesical pressure, $(P_{ves})$, and abdominal pressure, $(P_{abd})$. $P_{ves}$ is measured with a catheter placed in the bladder while $P_{abd}$ is measured with a cateter placed in the rectum or vagina. The rectum is in close proximity to the bladder, thus the intra-abdominal pressure experienced by both is theoretically similar, allowing detrusor pressure, $(P_{det})$, to be estimated as a subtracted value $P_{det} = P_{ves} - P_{abd}$. It is created by both active (bladder contractions) and passive (elasticity) forces from the bladder wall. Changes in passive forces may be caused by a loss of bladder compliance, and changes in active forces may result from muscular or neurogenic events [16], [11], [10].

Before staring the infusion of the fluid and measure pressures within the bladder, it is necessary to measure the "zero pressure", which corresponds to the surrounding atmospheric pressure, and is measured with the transducer open or with the open end of a connected, fluidfilled tube positioned outside the bladder at the same level as the bladder. The same reference level, the upper edge of the pubic symphysis, must be used for the pressure transducers, for the bladder and rectal catheters.

The rectal catheter should be zeroed to equal bladder pressure at the start of the study and generally it is placed beyond the anal sphincter so as to avoid interference in pressure measurement caused by rectal contractions, that may be correlated with detrusor overactivity. The patient should cough periodically during cystometry to ensure accurate pressure recording in all channels monitored, demonstrating a rise in rectal pressure and a rise in vesical pressure, with no change in detrusor pressure [16], [11], [10].

Then the bladder is filled with filling medium typically at a supraphysiologic filling rate while the patient is asked to report when various sensations are experienced: first sensation of filling (FSF), first desire to void (FDV), strong desire to void (SDV), symptoms of urge, and pain. The bladder is filled until maximum cystometric capacity (MCC) is reached. In the normal case MCC is the volume at which the patient states that he/she can no longer delay micturition because of SDV or urgency. In urge incontinence, MCC is the volume at which involuntary voiding occurs and in the absence of sensation cystometric capacity, is the volume at which the investigator decides to finish filling [16], [11], [10].

Interpretation of multichannel cystometrics requires knowledge of the normal filling parameters. The International Consultation on Incontinence recommends that in general the following guidelines should be used for interpretation (Urodynamic Testing, Urodynamics, M148):

- FSF at 170–200 cc;
- FDV at 250 cc;
- SDV at 400 cc;
- MCC at 480 cc.

Based on these parameters, increased bladder sensation is defined as sensations that occur at a lower bladder volume than what would normally be expected, while reduced bladder sensation is defined as sensations that occur at a higher bladder volume than what would normally be expected. Additionally, the $P_{det}$ during filling should remain low and constant. Rises in $P_{det}$ indicate decreased compliance and must be noted. Compliance is a measure of the viscoelastic property of the bladder, representing the ability of the urinary bladder to stretch in response to pressure. It is calculated with results from the cystometrogram by dividing the volume change by the change in $P_{det}$. According to Dorland's Medical Dictionary the normal bladder has a compliance of no more than 2 cm increase of water pressure per 100 mL of fluid, or 50 mL/cm$H_2O$ [16], [11], [10].

A normal or stable tracing should be absent of any detrusor contractions. An example of an ideal cystometric trace is shown in Figure 3.1. According to the ICS, any contraction during the course of cystometry that gives the patient the feeling he needs to void, is considered bladder overactivity. It is important to report the number of detrusor contractions, the respective volume, and pressure amplitude. An example of a low compliant bladder and an overactive detrusor is shown in Figure 3.2 [16], [11], [10].

As with all urodynamic tests, the results obtained from filling cystometry can be highly variable, depending on various technical aspects and differences in interpretation.

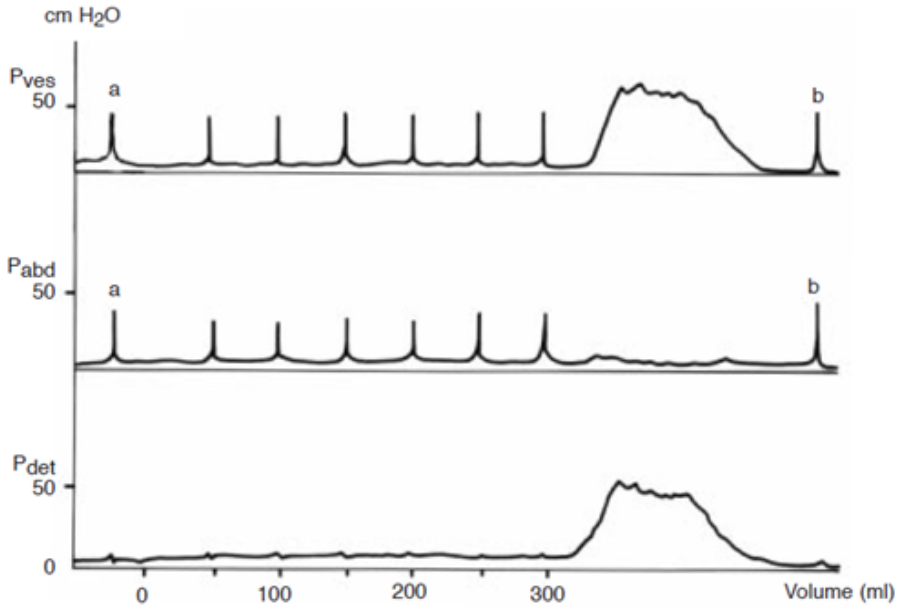


Figure 3.1: Ideal cystometric traces with coughing at regular intervals of 50mL filling. Note coughs before starting $(a)$ and after ending the test $(b)$ [11].

## 3.3 Uroflowmetry

Uroflowmetry, or uroflow, is a noninvasive urodynamic test that measures the rate of flow of urine expelled via the urethra during voiding. It gives an assessment of voiding in a simple and relatively inexpensive way [11].

It is a simple test to perform especially in patients with voiding dysfunction. The patient is asked to void upon the normal desire feeling into an electronic volume detector that measures weight changes over time [11].

Normal bladder voiding occurs with the contraction of the detrusor with coordinated relaxation of bladder neck. A graphical representation of the flow pattern is generated. Normal micturation presents low pressure and can be represented by a flow curve that is smooth and arc-shaped [11].

In Figure 3.3 is shown the expected pattern of normal flow: continuous, bell-shaped smooth curve, with rapidly increasing flow rate. Several objective values are calculated: flow rate (volume expelled per unit of time), maximum flow rate, $(Q_{\max})$, and total voided volume [11].

Different studies have established maximum urine flow rates to be greater than 12 mL/s. Due to the short urethra in females, and minimal outlet resistance, the leading factors affecting the uroflow in women are the detrusor strength, urethral resistance and the sphincter relaxation. In a normal woman maximum flow can be greater than 30 mL/s. Abnormally slow flow rates have been determined as under the tenth percentile of the Liverpool nomogram, presented in Figure 3.4, which takes into account the voided volume [16], [11].

Abnormalities in the flow pattern or rate can be due to various pathologies. In general, factors that affect passive relaxation of the bladder neck, urethral resistance or detrusor contractility

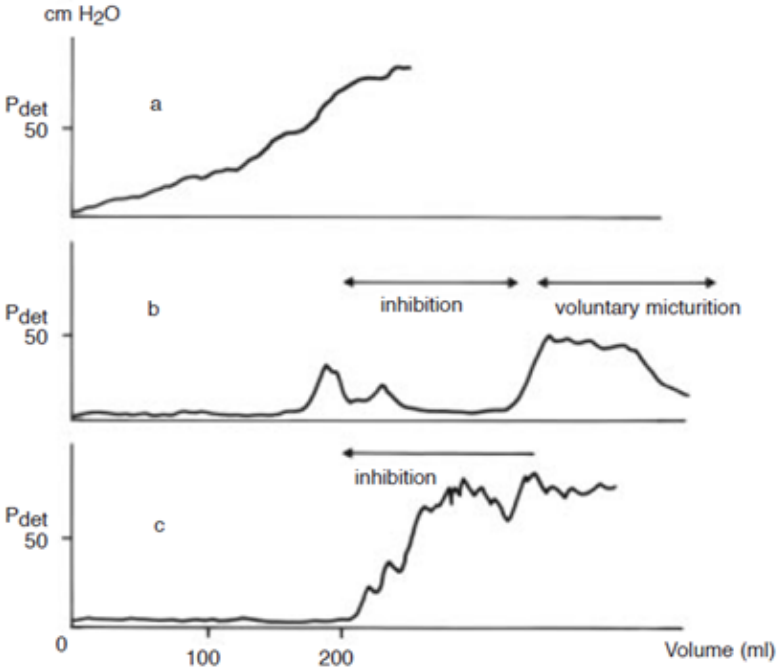


Figure 3.2: Diagrams to show low compliant bladder $(a)$, overactive detrusor with phasic pressure waves that the patient can supress $(b)$, and overactive detrusor with subsequent leakage that the patient cannot supress $(c)$ [11].

will change the uroflowmetric parameters. Flow patterns with episodes of increase, decrease and interruption are related to patients that present detrusor sphincter dyssynergia, where there is the spasm of the external sphincter [16], [11].

Interpretation of uroflowmetry is highly dependent on the voided volume, thus it is important to ensure that the micturition is representative. If possible, a voided volume of at least 150 mL, and preferably 200 mL (correspondingly less in children: 50 mL or more) should be obtained. At least two uroflowmetries should be performed when obstruction is suspected, since a single flow can be misleading [16], [11].

Usually, the volume of residual urine should be very small. In adults, values about 100 mL or more are considered abnormal. In children, a residual urine volume greater than about 10% of the maximum cystometric bladder capacity may be considered elevated. In the elderly, residual urine volumes of about 100 mL are common and may be acceptable, although they may affect choice of treatment for incontinence [16], [11].

When a normal $Q_{\max}$ and a normal voided volume without residual urine are present, in either female or male, infravesical obstruction or reduced detrusor contractility is unlikely [16], [11].

A first diagnosis can be obtained through the analysis of the flow pattern and the objective values stated above, but further validation with further clinical tests is required. Uroflowmetry should be performed prior to any urethral instrumentation [16], [11].

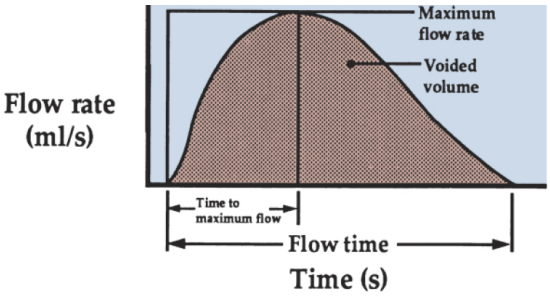


Figure 3.3: Schematic curve of normal flow [10].

## 3.4 Post-void Residual

The simplest evaluation of bladder emptying is to obtain a PVR, the volume of urine that remains in the bladder after micturition, either after passive or active filling of the bladder. Techniques for determining PVR include ultrasonic techniques or catheterization [16].

In spite of being the least invasive, ultrasonic techniques are indirect measures of volume based on measurements on several axis that may introduce error. Direct measurement, utilizing a catheter, provides the most accurate measure of PVR [16].

Normal values for PVR are often quoted as values less than 50–100 cc. Naturally, an isolated finding of an elevated PVR should be interpreted with caution, as variation in PVRs can be due to either patient or equipment factors. It is important to ensure that an abnormal PVR is found on repetitive testing. A high PVR often indicates incomplete voiding due to either poor detrusor contractility or outlet obstruction and should prompt further investigation [16].

## 3.5 Pressure-flow Study

Pressure-flow study combines the basic principles of uroflowmetry with the addition of abdominal and bladder pressure measurements. This combination allows evaluation of the pressures that are being generated during the voiding phase, therefore allowing the clinician to examine the pressure volume relationship during micturition [16], [11].

The goal of interpreting a pressure-flow study is to assess whether the neurologic mechanism of micturition is intact. This includes the ability of the detrusor muscle to contract and generate an appropriate voiding pressure, the urethral sphincter to relax, and that the timing of these events are coordinated to provide a smooth continuous flow. Measurements obtained during a pressure-flow study include premicturition pressure, opening time, opening pressure, maximum pressure, pressure at maximum flow, closing pressure, contraction pressure at maximum flow and flow delay [16], [11].

In general, abnormalities in a pressure-flow study can be classified into three general groups of pathologies including detrusor contractility issues, bladder outlet obstructions or neurophysiologic abnormalities. Therefore a free uroflowmetry and a determination of post-void residual urine

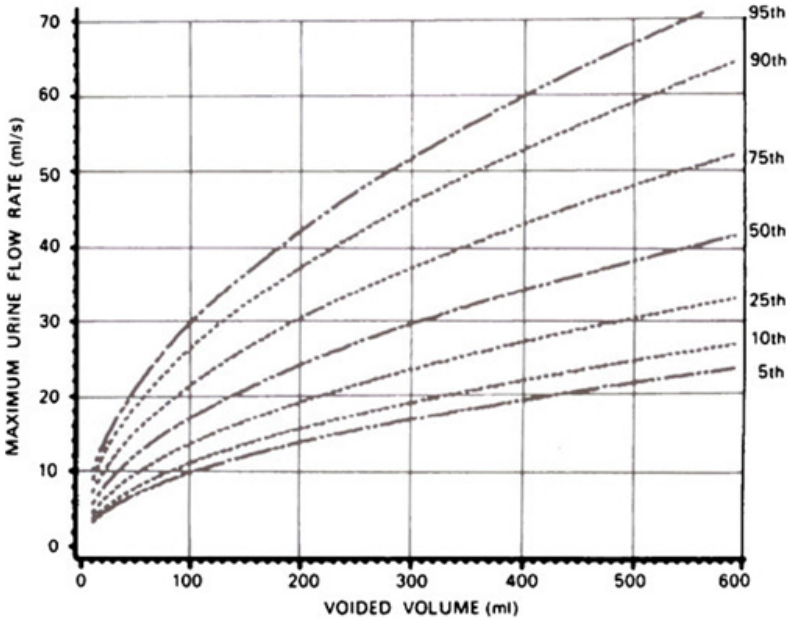


Figure 3.4: Liverpool nomogram for maximum urine flow rate in women [12].

should always precede pressure-flow studies. If the free uroflow is normal with no significant residual urine there is usually no indication for a pressure-flow study. On the other hand, if the free uroflow is abnormal and/or there is elevated residual urine, a pressure-flow study may be performed in order to distinguish between urethral obstruction and detrusor underactivity, or to help distinguish between neuropathy and a structural urethral obstruction as the cause of detrusor overactivity and related symptoms [16], [11].

Evaluation of the voiding $P_{\text{det}}$ and flow rate can help the practioner delineate the potential cause. Abnormal pressure-flow studies usually fall under two general patterns: low flow rate and an elevated $P_{\text{det}}$, suggestive of bladder outlet obstruction; low flow rate and low $P_{\text{det}}$, suggesting potential contractility issue with the detrusor muscle. Based on several previous studies bladder outlet obstruction is defined as the presence of a free $Q_{\text{max}} < 12$ mL/s and $P_{\text{det}} > 20$ cm $H_2O$ in a pressure-flow study [16], [11].

As pressure-flow studies are concerned with voiding, they do not usually address incontinence directly. Although a pressure-flow study may confirm suspected detrusor underactivity and thus to help to warn patients who potentially may encounter post-operative voiding difficulty, if incontinence surgery is being considered, there is no evidence that it is a more reliable predictor of voiding difficulty than uroflowmetry and residual urine determination. The evidence that pressure-flow studies can improve the outcome of incontinence treatment is yet very limited [16], [11].

## 3.6 Urethral Pressure Profile

Urethral pressure profile (UPP) is a test that attempts to measure the urethral pressure throughout the length of the urethra during rest. Two measurements of urethral pressure are performed: static urethral pressure profile (static UPP) and micturitional urethral pressure profile (micturational UPP). The first is performed with the patient at rest, as suggested by its name, while in the latter the patient is asked to void during the catheter withdrawn [16], [11].

UPP involves placement of a urethral pressure catheter that will measure the intraluminal pressure as the catheter is withdrawn at a constant rate of speed. While less commonly used nowadays, the goal of UPP is to distinguish between intrinsic sphincter deficiency (ISD) from SUI. In order to maintain continence the urethral lumen should seal completely, thus urethral resistance must exceed the forces of urinary expulsion. This hermetic effect is dependent upon the softness and compressibility of the urethral wall. Together, these properties determine the intraluminal urethral pressure [16], [11].

Several objective measurements including maximum urethral pressure (MUP), urethral closure pressure profile (UCPP), maximum urethral closure pressure (MUCP), functional profile length and pressure "transmission" ratio are measured in order to assess the urethral closure mechanism. MUCP is calculated by taking the difference between MUP and $P_{\text{ves}}$, and conceptually, therefore, it represents the ability of the urethra to prevent urine leakage. In Figure 3.5 is presented an example of a diagram of a female resting and stress urethral pressure profile indicating the objective measurements stated above [16], [11].

Urethral pressure measurements may be taken from all points along the urethra in steady-state conditions, and are reproduced in the form of a profile (the resting urethral pressure profile or the stress profile). Alternatively, the measurement may be made at one or more points along the urethra over a period of time during which conditions may be changing. The results may be presented in the form of a continuous trace (continuous urethrocystometry) or as a profile (the micturitional pressure profile) [16], [11].

Urethral pressures may be measured by perfusion techniques, by catheter-mounted microtransducers or by catheter-mounted balloons connected to an external transducer. All three methods have advantages and disadvantages. One problem is that, for any technique that uses sideholes or a side-mounted transducer, the measured "pressure" is liable to show an artifactual dependence on the orientation of the sidehole(s) or transducer. This behavior depends on the stiffness of the catheter and may lead to gross artifacts. It can be minimized by choosing a very flexible catheter or a catheter with multiple sideholes or sensors [16], [11].

Naturally, urethral pressure varies with bladder volume and with position. In continent women urethral closure pressure tends to increase with increasing volume and usually increases on assuming the erect position, whereas in stress incontinent women it tends to decrease with increasing volume and there is either no change or a decrease in pressure on standing [16], [11].

In practice, urethral pressures are usually determined during the filling or storage phases of the micturition cycle, when the urethra is empty and collapsed. As a consequence, difficulties arise

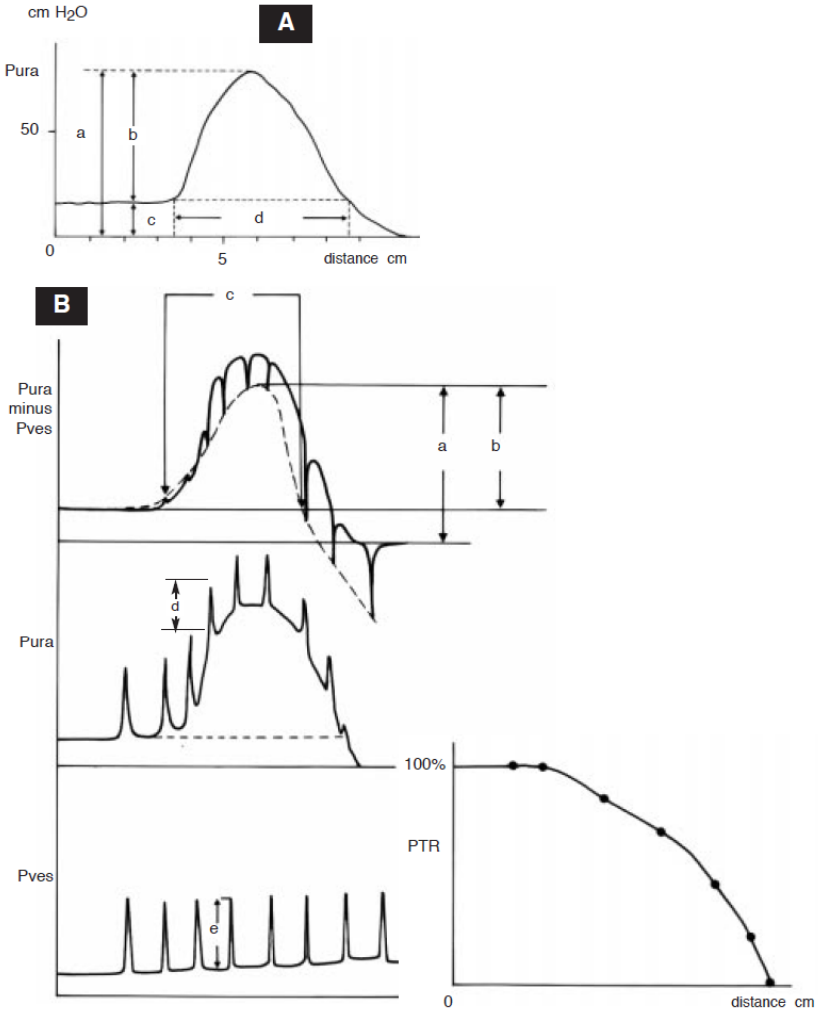


Figure 3.5: A : Diagram of a female resting urethral pressure profile indicating maximum urethral pressure (a), maximum urethral closure pressure (b), intravesical pressure (c), and functional profile length (d). B: Diagram of a female stress urethral pressure profile indicating maximum urethral pressure (stress) (a), maximum urethral closure pressure (stress) (b), and functional profile length (stress) (c). Pressure transmission ratio (PTR) is calculated as d/e [11].

in understanding, defining, and quantifying exactly what is being measured. However, urethral pressure may also be determined during micturition (micturitional UPP), as stated above. In this case, the main goal is to identify the presence and location of bladder outlet obstruction. For this purpose, bladder pressure is compared with urethral pressure along the urethra, and should be isobaric to the urethral one [16], [11].

As far as urethral obstruction is concerned, the pressure distal to the obstruction is lower than the proximal pressure, therefore a significant drop in pressure denotes the obstruction location. Nevertheless, in males with normal urinary flow rates, the urethral pressure drops significantly across the membranous-bulbous urethral region and continues to decline along the urethra. During normal voiding, this physiologic pressure drop is 20 to 30 cm $H_2O$ with detrusor contraction of 50

to 55 cm $H_2O$. In female, there is no significant pressure drop [16], [11].

## 3.7 Leak Point Pressure

The ability of the urethra to prevent the involuntary leakage of urine can also be evaluated by measuring the leak point pressure. Under normal physiologic and functional conditions, the urethral resistance should generate enough pressure to compensate for any abdominal or detrusor pressure that would be experienced through normal activities [16], [11].

Leak point pressure is defined as the lowest detrusor $(P_{det})$ or intravesical pressure $(P_{ves})$ at which involuntary expulsion of urine from the urethral meatus is observed. It is important to understand the difference between detrusor leak point pressure (DLPP) and abdominal leak point pressure (ALPP). DLPP is a static test that determines the lowest $P_{det}$ at which leakage of urine occurs in the absence of a detrusor contraction or increased abdominal pressure. On the other hand, ALPP is a dynamic test that determines the lowest $P_{ves}$ at which leakage occurs during an intentional increase in abdominal pressure (cough or Valsalva) [16], [11].

DLPP attempts to measure the ability of the urethra to resist increasing detrusor pressure. Unlike ALPP, DLPP is not used to evaluate SUI. Instead, it is related to bladder compliance and outlet resistance. ALPP attempts to assess the ability of the urethra to resist increased abdominal pressure, thus it is often used to evaluate SUI [16], [11].

Another aim of measuring DLPP is to assess the risk to the upper urinary tract. The critical cut-off value between high and low leak point pressure is approximately 40 cm H2O. Patients with neurogenic bladder dysfunction and a DLPP above this level are at risk for upper urinary tract deterioration [16], [11].

Regarding the ALPP, when obtained during coughing, it is performed by asking the patient to sequentially increase the intensity of cough in order to elicit leakage of urine. An alternative is to determine ALPP during a Valsalva maneuver. ALPP measured during a Valsalva maneuver may provide a more accurate measure of ALPP as it provides a more controlled rise in $P_{abd}$ as compared to the sharp rise in pressure obtained during coughing. For this reason, usually only in patients who fail to leak on a Vasalva maneuver a cough test is made. In Figure 3.6 is displayed an example of a detrusor and a Valsalva leak point pressure measurement [16], [11].

Several studies have attempted to use ALPP to differentiate between SUI due to urethral hypermobility and SUI due to ISD. Some practitioners suggest that a ALPP $<$ 60 cm $H_2O$ is correlated with ISD, while a ALPP greater than 90-100 cm $H_2O$ suggest that stress incontinence is associated with descent of the bladder base or so called "hypermobility", reflecting pelvic floor weakness [16], [11].

In spite of being possible to obtain an ALPP as a single urodynamic test, several studies have show that isolated ALPPs are not helpful as predictors of success for suburethral sling procedures in patients with SUI [16], [11].

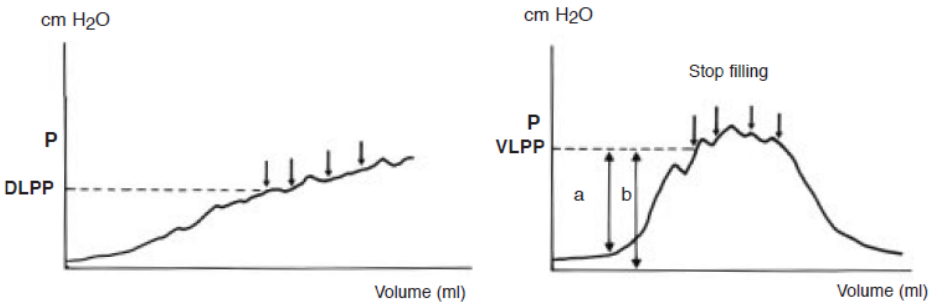


Figure 3.6: Measurement of detrusor leak point pressure (DLPP - left) and Valsalva leak point pressure (VLPP - right). The rise in pressure from the base line (a) or from the zero level (b) represents VLPP depending on the investigators. Arrows indicate leakage. [11].

## 3.8 Surface Electromyography

Electromyography (EMG) of the urethral sphincter, the anal sphincter, or the pelvic floor is another method for the diagnosis of lower urinary tract dysfunction. This non-evasive test provides two types of information: a simple indication of muscle behavior (the kinesiological EMG) and an electrical correlate of muscle pathology. The above procedures are performed using needle or wire electrodes (electrical correlate of muscle pathology) or needle electrodes or surface (patch) electrodes (the kinesiological EMG) [11].

EMG methods using needle electrodes are reserved for diagnostics in well selected groups of mainly neurogenic patients. A kinesiological EMG is normally attained with cystometry. The interpretation is limited to recording of gradually increasing EMG activity during filling of the bladder and of appropriate relaxation of the pelvic floor during voiding [11].

An incompetent urethral closure mechanism may be observed when there is reduced or none activity in the sphincter during the filling of the bladder. During the voiding phase, the EMG should become almost silent (sphincter relaxation), otherwise urethral function may be overactive. If the sphincter EMG waxes and wanes during this phase, it may indicate a functional obstruction (detrusor-sphincter dyssynergia in neurological conditions, dysfunctional voiding in non-neuropathic patients) and if an increase of EMC is observed, it may suggest abdominal straining [11].

Urodynamic studies can be performed both in an office and in a normal urodynamic setting. The last one is the appropriate to identify detrusor-sphincter dyssynergia [11].

## 3.9 Videourodynamics

Videourodynamics is an advanced urodynamic test used to evaluate complex urinary dysfunction. The test combines urodynamic investigations with X-ray or ultrasound real time images of the lower urinary tract during filling and voiding phase [11].

The patient's bladder should be empty before videourodynamic investigation. As it is filled with a catheter, the shape of the bladder shouldn't change, its neck should be closed and its base should be approximately level with the upper border of the *symphysis pubis*. During coughing or abdominal straining no changes should be observed and there shouldn't be any leakage. In the voiding phase the bladder neck opens, otherwise detrusor-bladder neck dyssynergia may exist. During filling the urethra should be closed and form a continuous flow voiding. The external urethral sphincter remains open without movement during voiding or detrusor-sphincter dyssynergia may be present [11].

Videourodynamics is used to define the cause of the incontinence, particularly in patients with neurogenic lower urinary tract dysfunction and incontinence, to provide concrete diagnoses to incontinent patients with other pathology when other methods of diagnosis fail to lead to solid diagnosis, or after failure of initial therapy based on less complicated methods of diagnosis [11].

The advantages of videourodynamics include direct documentation of incompetent bladder neck, inadequate urethral closure during filling, the location of urethral obstruction during voiding and dyssynergia between detrusor and external sphincter of bladder neck. Other diagnosis such as descent of the bladder base, bladder base hypermobility and intrinsic sphincter deficiency can immediately be distinguished. Incontinence can be determined fluoroscopically. Another advantage of videourodynamics is that any sign of reflux during the filling or voiding phase can be promptly identified and that anatomical malformations can be documented [11].

Videourodynamics provides additional information over traditional urodynamic studies but it is not recommended for most patients. These tests should be reserved for the most complex situations and they should not be considered a first line evaluation since they involve radiation exposure, they are very expensive and they may be more embarrassing and uncomfortable for the patient. Furthermore, the invasiveness of the study may adversely affect the functional results obtained [11].

Ultrasound videourodynamics has disadvantages too. It requires direct contact of the ultrasound transducer with the patient's body in the area of the lower urinary tract which may alter the anatomical conditions in this area. Using this procedure it is impossible to observe the upper urinary tract synchronously or to see the whole urethra [11].

Videourodynamics with fluoroscopy should be used only when simpler tests don't give a clear diagnosis or when complicated pathology is expected from the history and symptoms because of radiation exposure and because of the fact that this method may influence the lower urinary tract function and /or anatomy [11].

Videourodynamic study requires the same standard radiological precautions and procedures as filling cystometry and pressure-flow investigation [11].

## 3.10 Ambulatory Urodynamic Monitoring

Ambulatory urodynamic monitoring (AUM) is an established method of investigating lower urinary tract function in an ambulatory setting. This procedure is used when conventional urodynamic

investigation isn't enough to produce a clear diagnosis [11].

AUM frees the patient from medical staff and from fixed urodynamic equipment and offers the possibility of monitoring the detrusor function during which the bladder fills at natural rates while the patient is able to exercise and perform normal daily activities outside the clinical environment [11].

The urethral pressure may be recorded during AUM, otherwise the diagnostic sensibility for stress incontinence may be low and the diagnosis of an unstable urethra or that of low urethral closure pressure is less possible to achieve. Recording of flow during micturition enables pressure to be related to low flow rate [11].

The study results of conventional cystometry and AUM are often different. The published literature regarding measurement variation suggests that the number of detrusor contraction increases, voiding volume is lower and the values for voiding pressure and micturition flow rate are higher with AUM compared to conventional cystometry. Furthermore, during AUM it was observed a significantly increase frequency of phasic detrusor contractions and a low end-filling pressure in patients with neuropathic conditions and low compliance during conventional cystometry. Thus, low compliance may be attributable to an artifact of the different filling rate during conventional cystometry [11].

Using AUM, the detrusor pressures during the voiding phase consists of two waves, being the second wave or "after contraction" larger than the first. This may be the result of a physiological phenomenon or of the contact between the collapsed bladder wall and the microtip transducer and thus be an artifact. The catheters used to record abdominal pressure mal also record artifacts due to kinking of the catheter in the vagina or to rectal contractions, respectively. To a decrease in the vaginal pressure, corresponds an increase in detrusor pressure which may be wrongly understood as a detrusor contraction [11].

When recording the urethral pressure, the closure pressure may decrease to zero as a result of the displacement of the urethral transducer out of the maximum urethral pressure zone. If there is no leakage together with a zero closure pressure, one must assume the displacement of the transducer [11].

AUM is a valuable and effective second-line investigation for diagnosing the cause of incontinence in difficult cases. It may be used with patients with mixed incontinence symptoms, or with those complaining incontinence without objective data of leakage. However, this method is not a very specific one to detect urine leakage and it may make interpretation difficult due to artifacts associated with catheter displacement [11].

# Chapter 4

# Continuum Mechanics

A material body in motion will have different configurations over time, therefore it is important to establish the equations of motion that allow us to characterize how the continuum evolves and how its properties, displacement, velocity, accelaration, change over time [18].

Motion of a continuous medium, also designated by deformation, is characterized by the following types [18]:

- Rigid body motion - the original shape of the body is maintained after motion. The distance between particles is preserved. It can be classified by translation and/or rotation;
- Motion with deformation - the distance between particles changes.

In general, motion is characterized by both deformation and rigid body motion simultaneously. In order to characterize a material body's motion it is usually adopted two types of configurations [18]:

- The reference configuration or the initial configuration - the configuration at the instant of time $(t = 0 \equiv t_0)$ is considered to be the undeformed configuration in which the particle $P$ is identified by the position vector $\mathbf{X_P}$;
- The current configuration or deformed configuration - the configuration at the instant of time $t$.

## 4.1 Description of Motion

If we consider a material body, Figure 4.1, $\mathbf{B_0}$ in the initial configuration, at an arbitrary time $t$ the material body occupies a new position in space, $\mathbf{B_t}$, which can be expressed in the reference configuration as [18],

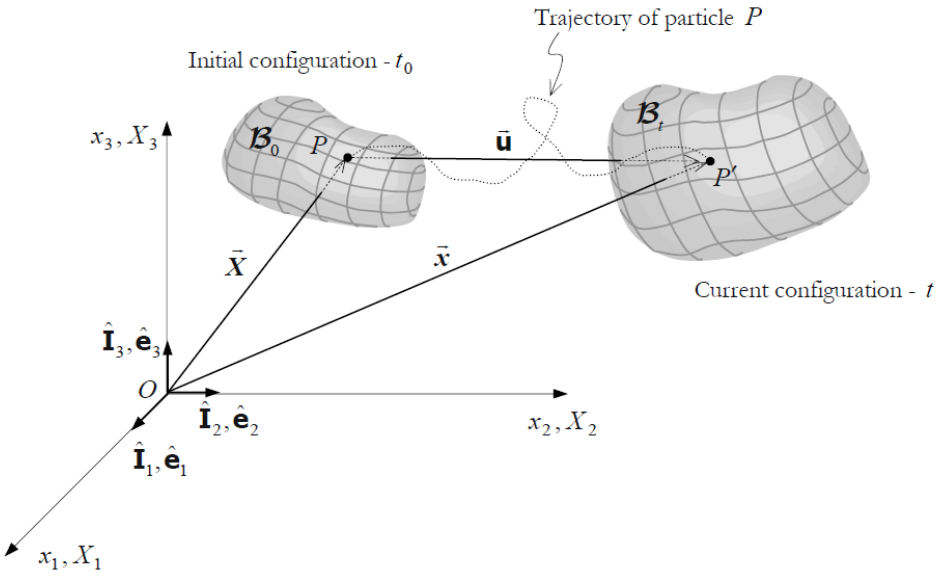


Figure 4.1: Initial and current configurations [18].

$$\mathbf{X} = X_1\mathbf{e_1} + X_2\mathbf{e_2} + X_3\mathbf{e_3} \tag{4.1}$$

which difines the material coordinate,

$$\mathbf{X_i} = \{X_1\ X_2\ X_3\}^T \tag{4.2}$$

In the current configuration particle $P$ occupies the position $P$' and the position vector is given by,

$$\mathbf{x} = x_1\mathbf{e_1} + x_2\mathbf{e_2} + x_3\mathbf{e_3} \tag{4.3}$$

which difines the spatial coordinate,

$$\mathbf{x_i} = \{x_1\ x_2\ x_3\}^T \tag{4.4}$$

At this point, it is possible to write the displacement, velocity and acceleration vectors. By definition the displacement vector, $\mathbf{u}$, of a particle is the difference between the position vector in the current configuration, $\mathbf{x}$, and the position vector in the reference configuration, $\mathbf{X}$ [18],

$$\mathbf{u} = \mathbf{x} - \mathbf{X} \tag{4.5}$$

As far as the velocity and acceleration vectors are concerned, the first is defined by the rate of change of the position vector and the second is the rate of change of velocity [18],

$$\mathbf{V} = \frac{d\mathbf{x}}{dt} = \dot{\mathbf{x}} = \frac{d(\mathbf{u}+\mathbf{X})}{dt} = \frac{d\mathbf{u}}{dt} = \dot{\mathbf{u}} \tag{4.6}$$

$$\mathbf{A} = \frac{d\mathbf{V}}{dt} = \dot{\mathbf{V}} = \frac{d^2\mathbf{x}}{dt^2} = \ddot{\mathbf{u}} \tag{4.7}$$

It is possible to correlate continuum properties between the current and reference configurations, hence the study of motion can be carried out either in the current or reference configuration [18]. If the particle in motion is described in terms of material coordinates, $\mathbf{X}$, and time as [18],

$$\mathbf{x} = \mathbf{x}(\mathbf{X}, t) \tag{4.8}$$

it is called Lagrangian or material description of the motion. On the other hand, if the particle of motion is described in terms of spatial coordinates, $\mathbf{x}$, and time as [18],

$$\mathbf{X} = \mathbf{X}(\mathbf{x}, t) \tag{4.9}$$

it is called the eulerian description of motion.

Depending on whether a property is a Lagrangian or Eulerian variable, its material time derivative is expressed differently. In Lagrangian description the material time derivative of a property $\theta$ is expressed as [18],

$$\dot{\theta}(\mathbf{X}, t) = \frac{D\theta(\mathbf{X}, t)}{Dt} = \frac{d\theta(\mathbf{X}, t)}{dt} \tag{4.10}$$

If the property is in Eulerian description, the observer is not traveling with the particle, but fixed at one point. Thus, he only has information on the local rate of change. In order to be fully informed, it is necessary to know how the property of the particle changes along its path line, which is related to mass transport and is known as the convective rate of change. In equation 4.11 the first term represents the local rate of change and the second the convective rate of change [18].

$$\dot{\theta}(\mathbf{x}, t) = \frac{D\theta(\mathbf{x}, t)}{Dt} = \frac{\partial\theta(\mathbf{x}, t)}{\partial t} + \frac{\partial\theta(\mathbf{x}, t)}{\partial x_k}\frac{\partial x_k(\mathbf{X}, t)}{\partial t} = \frac{\partial\theta(\mathbf{x}, t)}{\partial t} + \frac{\partial\theta(\mathbf{x}, t)}{\partial x_k} v_k(\mathbf{X}, t) \tag{4.11}$$

Then it is possible to express the material time derivative operator for an Eulerian property, $\bullet(\mathbf{x}, t)$, as [18],

$$\frac{D\bullet(\mathbf{x}, t)}{Dt} = \frac{\partial\bullet(\mathbf{x}, t)}{\partial t} + \nabla_x \bullet(\mathbf{x}, t) \cdot \mathbf{v}(\mathbf{x}, t) \tag{4.12}$$

## 4.2 The Deformation Gradient

In order to define some deformation and strain tensors, analyzing how distances between particles change during motion is required. Considering two particles in the reference configuration shown in Figure 4.2, which are denoted by $P$ and $Q$, $d\mathbf{X}$ is a vector joining both points and $\mathbf{M}$ is the unit vector associated with the $d\mathbf{X}$ direction. After motion both particles $P$ and $Q$ occupy new positions

$P'$ and $Q'$, respectively. In this new configuration, current configuration, the vector joining both points is represented by $d\mathbf{x}$. This vector is associated with the unit vector $\mathbf{m}$ [18].

The magnitudes of $d\mathbf{X}$ and $d\mathbf{x}$ are expressed, respectively, by,

$$\|\overrightarrow{PQ}\| = \|d\mathbf{X}\| = dS \tag{4.13}$$

$$\|\overrightarrow{P'Q'}\| = \|d\mathbf{x}\| = ds \tag{4.14}$$

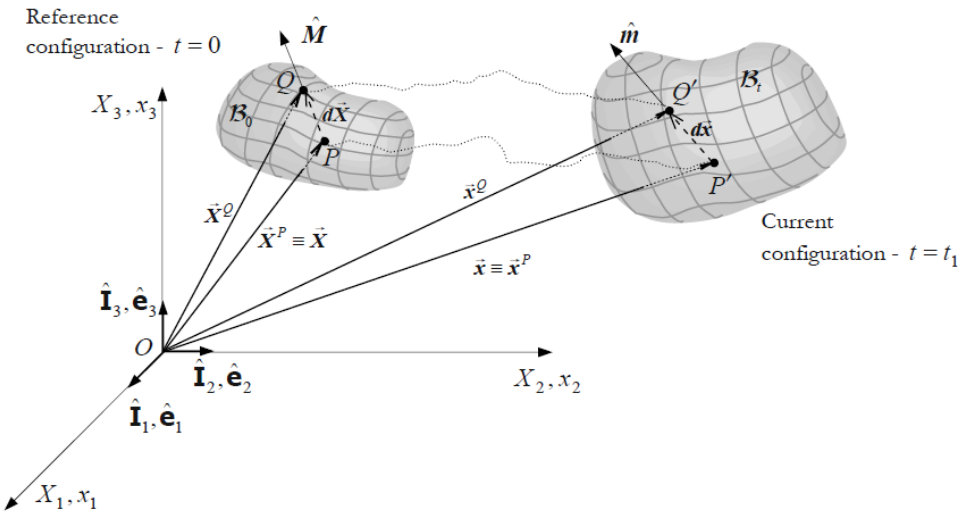


Figure 4.2: Continuum deformation [18].

It is possible to define two parameters - stretch, $\lambda_{\mathbf{m}}$, associated with the $\mathbf{m}$ direction and the unit extension, $\varepsilon_{\mathbf{m}}$ [18],

$$\lambda_{\mathbf{m}} = \frac{\|d\mathbf{x}\|}{\|d\mathbf{X}\|} = \frac{ds}{dS} \tag{4.15}$$

$$\varepsilon_{\mathbf{m}} = \frac{\|d\mathbf{x}\| - \|d\mathbf{X}\|}{\|d\mathbf{X}\|} = \frac{ds - dS}{dS} \tag{4.16}$$

The deformation gradient can be obtained by finding a relationship between $d\mathbf{X}$ and $d\mathbf{x}$. By considering the material description of motion, applying vector addition and Taylor series it is possible to obtain the following relashionship [18],

$$d\mathbf{x} = \mathbf{F}d\mathbf{X} \tag{4.17}$$

where $\mathbf{F}$ is a two-point tensor, known as the material deformation grafient or deformation gradient. Its material time derivative is expressed as [18],

$$\dot{\mathbf{F}} = \boldsymbol{\ell} \cdot \mathbf{F} \tag{4.18}$$

where $\boldsymbol{\ell}$ is the spatial velocity gradient, which is defined as [18],

$$\boldsymbol{\ell}(\mathbf{x},t) = \nabla_{\mathbf{x}}\mathbf{v}(\mathbf{x},t) = \dot{\mathbf{F}}\cdot\mathbf{F}^{-1} \tag{4.19}$$

and can be decomposed into a symmetric and an antisymmetric part [18],

$$\boldsymbol{\ell} = \boldsymbol{\ell}^{sym} + \boldsymbol{\ell}^{skew} = \frac{1}{2}(\boldsymbol{\ell}+\boldsymbol{\ell}^{T}) + \frac{1}{2}(\boldsymbol{\ell}-\boldsymbol{\ell}^{T}) = \mathbf{D}+\mathbf{W} \tag{4.20}$$

where $\boldsymbol{\ell}^{sym} = \mathbf{D}$ and $\boldsymbol{\ell}^{skew} = \mathbf{W}$. $\mathbf{D}$ represents the rate of deformation tensor and $\mathbf{W}$ the spin, rate of rotation tensor [18].

Considering the displacement field $\mathbf{u}$ and its components in Lagrangian description and taking the partial derivative of it with respect to the material coordinates $\mathbf{X}$, the material displacement gradient tensor, $\mathbf{J}$, is obtained [18],

$$\nabla_{\mathbf{X}}\mathbf{u}(\mathbf{X},t) = \mathbf{F}-\mathbf{1} = \mathbf{J}(\mathbf{X},t) \tag{4.21}$$

The material displacement gradient tensor is related to the spatial displacement gradient tensor, $\mathbf{j}$, by [18],

$$\mathbf{J}(\mathbf{X},t) = \mathbf{j}(\mathbf{x},t)\mathbf{F} \tag{4.22}$$

## 4.3 Finite Strain Tensors

Regarding the Figure 4.2 and equations 4.13 and 4.14 it is possible to establish a relashionship between $(ds)^2$ and $(dS)^2$ in the material description [18],

$$(ds)^2 - (dS)^2 = d\mathbf{X}\cdot(\mathbf{F}^T\cdot\mathbf{F}-\mathbf{1})\cdot d\mathbf{X} = d\mathbf{X}\cdot(\mathbf{C}-\mathbf{1})\cdot d\mathbf{X} = d\mathbf{X}\cdot(2\mathbf{E})\cdot d\mathbf{X} \tag{4.23}$$

where $\mathbf{C}$ is known as the right Cauchy-Green deformation tensor or Green deformation tensor and is defined as [18],

$$\mathbf{C}(\mathbf{X},t) = \mathbf{F}^T\cdot\mathbf{F} \tag{4.24}$$

and $\mathbf{E}$ is the Green-Lagrange strain tensor or Lagrangian finite strain tensor. $\mathbf{C}$ is a symmetric tensor, i.e. $\mathbf{C}^T = \mathbf{C}$, and since $|F| \neq 0$ is also positive definite tensor. The inverse of $\mathbf{C}$, also in the reference configuration, is [18],

$$\mathbf{C}^{-1}(\mathbf{X},t) = \mathbf{F}^{-1}\cdot\mathbf{F}^{-T} \tag{4.25}$$

In the spatial configuration, it is possible to write the left Cauchy-Green deformation tensor, **b**, which is a positive definite symmetric tensor [18],

$$\mathbf{b}(\mathbf{x},t) = \mathbf{F}\cdot\mathbf{F}^T \tag{4.26}$$

The inverse of **b** is given by,

$$\mathbf{b}^{-1}(\mathbf{x},t) = \mathbf{F}^{-T}\cdot\mathbf{F}^{-1} \tag{4.27}$$

Finally, the Green-Lagrange strain tensor is defined as [18],

$$\mathbf{E}(\mathbf{X},t) = \frac{1}{2}(\mathbf{F}^T\cdot\mathbf{F}-\mathbf{1}) = \frac{1}{2}(\mathbf{C}-\mathbf{1}) \tag{4.28}$$

The Green-Lagrange strain tensor is also a symmetric tensor and can be also expressed in function of the material displacement gradient tensor, **J** [18],

$$\mathbf{E} = \frac{1}{2}(\mathbf{J}+\mathbf{J}^T+\mathbf{J}^T\cdot\mathbf{J}) \tag{4.29}$$

It is possible to establish a relashionship between the Green-Lagrange strain tensor and the Eulerian finite strain tensor or Almansi strain tensor, **e** [18],

$$\mathbf{E} = \mathbf{F}^T\cdot\mathbf{e}\cdot\mathbf{F} \tag{4.30}$$

Both **E** and **e** are symmetric second-order tensors. The material time derivative of the right Cauchy-Green deformation tensor, **C**, and the Green-Lagrange strain tensor, **E**, can be expressed by [18],

$$\dot{\mathbf{C}} = 2\mathbf{F}^T\cdot\mathbf{D}\cdot\mathbf{F} \tag{4.31}$$

$$\dot{\mathbf{E}} = \frac{1}{2}\dot{\mathbf{C}} = \mathbf{F}^T\cdot\mathbf{D}\cdot\mathbf{F} \tag{4.32}$$

## 4.4 Polar Decomposition of F

Using the polar decomposition theorem a non-singular second order tensor can be decomposed multiplicatively. By applying it to the deformation gradient **F** one obtain [18],

$$\mathbf{F} = \mathbf{R}\cdot\mathbf{U} = \mathbf{V}\cdot\mathbf{R} \tag{4.33}$$

where $\mathbf{R}\cdot\mathbf{U}$ is the right polar decomposition, $\mathbf{V}\cdot\mathbf{R}$ is the left polar decomposition and **R** is a proper orthogonal tensor. This tensor must meet two restrictions: $\mathbf{R}^T\cdot\mathbf{R} = \mathbf{R}\cdot\mathbf{R}^T = \mathbf{1} \Rightarrow \mathbf{R}^T = \mathbf{R}^{-1}$ and $det(\mathbf{R}) = 1$. **U** and **V** are symmetric positive definite tensors, known as the right stretch tensor (the Lagrangian stretch tensor or the material stretch tensor) and the left stretch tensor (the Eulerian stretch tensor or the spatial stretch tensor), respectively [18].

Taking the polar decomposition of $\mathbf{F}$ into account, it is possible to express the right Cauchy-Green deformation tensor, $\mathbf{C}$, as [18],

$$\mathbf{C} = \mathbf{U} \cdot \mathbf{U} = \mathbf{U}^2 \tag{4.34}$$

and the left Cauchy-Green deformation tensor, $\mathbf{b}$, as [18],

$$\mathbf{b} = \mathbf{V} \cdot \mathbf{V} = \mathbf{V}^2 \tag{4.35}$$

The tensors $\mathbf{C}$ and $\mathbf{b}$ are interrelated to each other by [18],

$$\begin{aligned} \mathbf{U} &= \mathbf{R}^T \cdot \mathbf{V} \cdot \mathbf{R} \\ \mathbf{V} &= \mathbf{R} \cdot \mathbf{U} \cdot \mathbf{R}^T \end{aligned} \tag{4.36}$$

## 4.5 Spectral Representation of Kinematic Tensors

The eigenvalues of $\mathbf{U}$ represent the principal stretches, $\lambda_i$. Each of them is associated with a principal direction $\mathbf{N}^{(i)}$ [18],

$$\begin{aligned} &\text{for} \quad \lambda_1 \Rightarrow \mathbf{N}^1 = [N_1^{(1)}\, N_2^{(1)}\, N_3^{(1)}] \\ &\text{for} \quad \lambda_2 \Rightarrow \mathbf{N}^2 = [N_1^{(2)}\, N_2^{(2)}\, N_3^{(2)}] \\ &\text{for} \quad \lambda_3 \Rightarrow \mathbf{N}^3 = [N_1^{(3)}\, N_2^{(3)}\, N_3^{(3)}] \end{aligned} \tag{4.37}$$

Thus, the spectral representation of $\mathbf{U}$ is given by [18],

$$\mathbf{U} = \sum_{a=1}^{3} \lambda_a\, \mathbf{N}^{(a)} \otimes \mathbf{N}^{(a)} \tag{4.38}$$

Therefore, the spectral representation of the right Cauchy-Green deformation tensor is [18],

$$\mathbf{C} = \mathbf{U}^2 = \sum_{a=1}^{3} \lambda_a^2\, \mathbf{N}^{(a)} \otimes \mathbf{N}^{(a)} \tag{4.39}$$

The spectral representation of the left stretch tensor and the left Cauchy-Green deformation tensor can also be obtained [18],

$$\mathbf{V} = \sum_{a=1}^{3} \lambda_a\, \mathbf{n}^{(a)} \otimes \mathbf{n}^{(a)} \tag{4.40}$$

$$\mathbf{b} = \mathbf{V}^2 = \sum_{a=1}^{3} \lambda_a^2\, \mathbf{n}^{(a)} \otimes \mathbf{n}^{(a)} \tag{4.41}$$

where $\mathbf{n}^{(a)} = \mathbf{R} \cdot \mathbf{N}$.

Finally, the spectral representation of the deformation gradient is given by [18],

$$\mathbf{F} = \sum_{a=1}^{3} \lambda_a \, \mathbf{n}^{(a)} \otimes \mathbf{N}^{(a)} \tag{4.42}$$

## 4.6 The Cauchy Stress Tensor

When a continuum is subjected to external forces the body is also subjected to internal forces, hence in order to characterize the stress state in the continuous medium, it is essential to define a continuous and differentiable tensor field to represent the internal forces [18].

According to Cauchy's fundamental postulate the traction $\mathbf{f}^{(\mathbf{n})}$ is a function of the position $(\mathbf{x})$ and the normal $(\mathbf{n})$. Considering Figure 4.3 the traction vector associated with the normal $\mathbf{n}$, in the current configuration, can be defined [18],

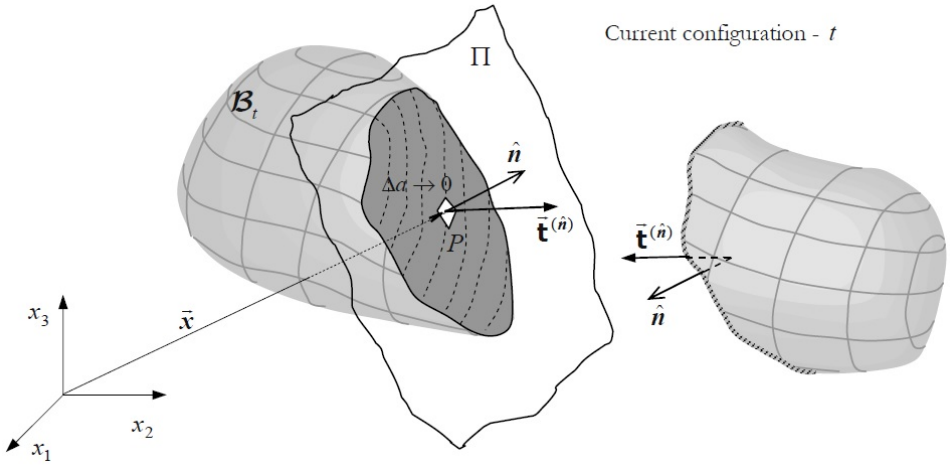


Figure 4.3: Traction vector [18].

$$\mathbf{t}^{(\mathbf{n})}(\mathbf{x},t,\mathbf{n}) = \lim_{\Delta a \to 0} \left( \frac{\Delta \mathbf{f}}{\Delta a} \right) \tag{4.43}$$

where $\Delta\mathbf{f}$ denotes the outcome of the internal force acting on the area element $\Delta a$, which is centered at the point $P(\mathbf{x},t)$ [18].

Knowing that the stress at a point $P(\mathbf{x},t)$ is completely described when the traction vector $\mathbf{t}(\mathbf{x},\mathbf{n})$ can be obtained for any arbitrary plane passing through the same point and that, according to Cauchy, if we define the traction vector on three mutually perpendicular planes passing through the point $P(\mathbf{x},t)$, the stress state at that point is fully described. It is possible to deduce the Cauchy stress tensor $\boldsymbol{\sigma}$ [18],

$$\boldsymbol{\sigma} = \sigma_{ij} \, (\mathbf{e}_i \otimes \mathbf{e}_j) \tag{4.44}$$

where $\sigma_{ij}$ is,

$$\sigma_{ij} = \begin{bmatrix} \sigma_{11} & \sigma_{12} & \sigma_{13} \\ \sigma_{21} & \sigma_{22} & \sigma_{23} \\ \sigma_{31} & \sigma_{32} & \sigma_{33} \end{bmatrix} \tag{4.45}$$

## 4.7 The First Piola-Kirchhoff Stress Tensor

The Cauchy stress tensor was derived in the current configuration, however in some cases it might be useful to adopt the Lagrangian description to study motion. In these cases, it is necessary to correlate the Cauchy stress tensor with a hypothetical stress tensor in the reference configuration [18].

After some manipulation it is possible to conclude that the first Piola-Kirchhof stress tensor, $\mathbf{P}$, is defined as [18],

$$\mathbf{P} = J\,\boldsymbol{\sigma}\cdot\mathbf{F}^{-T} \iff \boldsymbol{\sigma} = \frac{1}{J}\mathbf{P}\cdot\mathbf{F}^{T} \tag{4.46}$$

where $J$ is the Jacobian determinant.

This tensor is both a two-point second order tensor and a non-symmetric tensor since it represents the force in the current configuration per unit undeformed area [18].

## 4.8 The Kirchhoff Stress Tensor

The Kirchhoff stress tensor is related to the traction vector $\mathbf{t}$ (current configuration) and is defined as [18],

$$\boldsymbol{\tau} = J\boldsymbol{\sigma} \tag{4.47}$$

The Kirchhoff stress tensor is a symmetric second order tensor. It is related to the Cauchy stress tensor, equation 4.47, and the first Piola-Kirchhoff stress tensor by means of the following relationships [18],

$$\boldsymbol{\tau} = \mathbf{P}\cdot\mathbf{F}^{T} \tag{4.48}$$

$$\mathbf{P} = \mathbf{F}^{-1}\cdot\boldsymbol{\tau} \tag{4.49}$$

## 4.9 The Second Piola-Kirchhoff Stress Tensor

It is also possible to define another stress tensor denominated the second Piola-Kirchhoff stress tensor, $\mathbf{S}$, which is defined in the reference configuration as [18],

$$\mathbf{S} = \mathbf{F}^{-1}\cdot\mathbf{P} = \mathbf{F}^{-1}\cdot\boldsymbol{\tau}\cdot\mathbf{F}^{-T} = J\,\mathbf{F}^{-1}\cdot\boldsymbol{\sigma}\cdot\mathbf{F}^{-T} \tag{4.50}$$

or,

$$\mathbf{P} = \mathbf{F} \cdot \mathbf{S} \tag{4.51}$$

$$\boldsymbol{\tau} = \mathbf{P} \cdot \mathbf{F}^T = \mathbf{F} \cdot \mathbf{S} \cdot \mathbf{F}^T \tag{4.52}$$

The Cauchy stress tensor can be expressed in terms of the second Piola-Kirchhoff stress tensor as [18],

$$\boldsymbol{\sigma} = \frac{1}{J} \mathbf{F} \cdot \mathbf{S} \cdot \mathbf{F}^T \tag{4.53}$$

The second Piola-Kirchhoff stress tensor is also a symmetric tensor [18].

## 4.10 The Fundamental Equations of Continuum Mechanics

The fundamental equations of continuum mechanics are based on the conservation principles of certain physical quantities. They are summarized in table 4.1, in the current configuration [18].

Table 4.1: Fundamental equations of the continuum mechanics [18].

| **Fundamental Equations of the Continuum Mechanics (Current configuration)** | |
|---|---|
| Mass Continuity Equation (Principle of conservarion of mass) | $\frac{D\rho}{Dt} + \rho(\nabla_{\mathbf{x}} \cdot \mathbf{v}) = 0$ |
| Equation of Motion (Principle of conservation of linear momentum) | $\nabla_{\mathbf{x}} \cdot \boldsymbol{\sigma} + \rho \mathbf{b} = \rho \dot{\mathbf{v}}$ |
| Symmetry of the Cauchy Stress Tensor (Principle of conservation of angular momentum) | $\boldsymbol{\sigma} = \boldsymbol{\sigma}^T$ |
| Energy Equation (Principle of conservation of energy) | $\rho \dot{u} = \boldsymbol{\sigma} : \mathbf{D} - \nabla_{\mathbf{x}} \cdot \mathbf{q} + \rho r$ |
| Entropy Inequality (Principle of irreversibility) | $\rho \dot{\eta}(\mathbf{x},t) + \frac{1}{T}\boldsymbol{\sigma} : \mathbf{D} - \frac{1}{T}\rho \dot{u} - \frac{1}{T^2}\mathbf{q} \cdot \nabla_{\mathbf{x}} T \geq 0$ |

where $\rho$ is the mass density, $\mathbf{q}$ is the heat flux, $r$ is the radiant heat constant (also called heat source), $\eta$ is the specific entropy and, finally, $T$ is the absolute temperature [18].

## 4.11 Hyperelasticity

Some materials such as rubber and biological matter are classified as being hyperelastic. Purely hyperelastic materials have no memory of motion history, therefore they are only dependent on the current values of the state variables. Physically speaking, these materials return to their initial state once the load applied to them disappears - the work done during the loading process is recovered during the unloading process (it is a reversible process, there is no internal energy dissipation) [18].

A hyperelastic material supposes the existence of a function which is denoted by the Helmholtz free energy per unit reference volume, $\psi$, which is also known as strain energy density or the strain energy function or elastic potential. In these type of materials, the strain energy function is only dependent on the deformation gradient $\mathbf{F}$, $\psi = \psi(\mathbf{F})$ [18].

In pure deformation processes (there are no changes caused by entropy or temperature) internal energy dissipation is equal to zero [18],

$$\text{(Current configuration)} \quad \mathscr{D}_{int} = \boldsymbol{\sigma}:\mathbf{D} - \dot{\psi} = 0 \quad \Rightarrow \dot{\psi} = \boldsymbol{\sigma}:\mathbf{D} \tag{4.54}$$

$$\begin{aligned} \text{(Reference configuration)} \quad \mathscr{D}_{int} &= \mathbf{P}:\dot{\mathbf{F}} - \dot{\psi} = 0 \quad \Rightarrow \dot{\psi} = \mathbf{P}:\dot{\mathbf{F}} \\ \mathscr{D}_{int} &= \frac{1}{2}\mathbf{S}:\dot{\mathbf{C}} - \dot{\psi} = 0 \quad \Rightarrow \dot{\psi} = \frac{1}{2}\mathbf{S}:\dot{\mathbf{C}} \end{aligned} \tag{4.55}$$

It is possible to write the rate of change of the strain energy density as follows [18],

$$\dot{\psi} = \mathbf{P}:\dot{\mathbf{F}} = \mathbf{S}:\dot{\mathbf{E}} = \frac{1}{2}\mathbf{S}:\dot{\mathbf{C}} = \boldsymbol{\tau}:\mathbf{D} \tag{4.56}$$

Evaluating the rate of change of the strain energy $\psi(\mathbf{F})$ [18],

$$\dot{\psi}(\mathbf{F}) = \frac{\partial \psi(\mathbf{F})}{\partial \mathbf{F}}:\frac{\partial \mathbf{F}}{\partial t} = \frac{\partial \psi(\mathbf{F})}{\partial \mathbf{F}}:\dot{\mathbf{F}} \tag{4.57}$$

Substituting equation 4.57 into the internal energy dissipation given by the equations 4.54 and 4.55,

$$\mathbf{P}:\dot{\mathbf{F}} - \frac{\partial \psi(\mathbf{F})}{\partial \mathbf{F}}:\dot{\mathbf{F}} = 0 \quad \Rightarrow \quad \mathbf{P}:\dot{\mathbf{F}} = \frac{\partial \psi(\mathbf{F})}{\partial \mathbf{F}}:\dot{\mathbf{F}} \tag{4.58}$$

Thus,

$$\mathbf{P} = \frac{\partial \psi(\mathbf{F})}{\partial \mathbf{F}} \tag{4.59}$$

Strain energy has to be objective - $\psi(\mathbf{F}) = \psi(\mathbf{Q}\cdot\mathbf{F})$, where $\mathbf{Q}$ is an orthogonal tensor. Then, by applying the polar decomposition and adopting an orthogonal tensor, $\mathbf{Q} = \mathbf{R}^T$, it is possible to write the strain energy as a function of only the stretch tensor $\mathbf{U}$. Since $\mathbf{C}$, $\mathbf{U}$ and $\mathbf{E}$ are directly linked, the strain energy density can also be expressed in terms of the Green-Lagrange strain tensor, $\mathbf{E}$ [18].

Taking the rate of change of the energy $\psi(\mathbf{C})$ [18],

$$\dot{\psi}(\mathbf{C}) = \frac{\partial \psi(\mathbf{C})}{\partial \mathbf{C}}:\frac{\partial \mathbf{C}}{\partial t} = \frac{\partial \psi(\mathbf{C})}{\partial \mathbf{C}}:\dot{\mathbf{C}} \tag{4.60}$$

By substituting equation 4.60 into the internal energy dissipation (equation 4.55) [18],

$$\begin{aligned} \mathscr{D}_{int} &= \frac{1}{2}\mathbf{S}:\dot{\mathbf{C}} - \dot{\psi}(\mathbf{C}) = 0 \\ \mathscr{D}_{int} &= \frac{1}{2}\mathbf{S}:\dot{\mathbf{C}} - \frac{\partial \psi(\mathbf{C})}{\partial \mathbf{C}}:\dot{\mathbf{C}} = 0 \\ \mathscr{D}_{int} &= \left(\frac{1}{2}\mathbf{S} - \frac{\partial \psi(\mathbf{C})}{\partial \mathbf{C}}\right):\dot{\mathbf{C}} = 0 \end{aligned} \tag{4.61}$$

In a mechanical process with $\dot{\mathbf{C}} \neq 0$ the only scenario in which the condition 4.61 remains valid is when [18],

$$\frac{1}{2}\mathbf{S} - \frac{\partial \psi(\mathbf{C})}{\partial \mathbf{C}} = 0 \quad \Rightarrow \quad \mathbf{S} = 2\frac{\partial \psi(\mathbf{C})}{\partial \mathbf{C}} \tag{4.62}$$

Likewise, it is possible to deduce that [18],

$$\mathbf{S} = 2\frac{\partial \psi(\mathbf{C})}{\partial \mathbf{C}} = \frac{\partial \psi(\mathbf{E})}{\partial \mathbf{E}} \tag{4.63}$$

Taking into account the relationships between the stress tensors, the constitutive equation for stress can be expressed as follows [18],

- The Kirchhoff stress tensor ($\boldsymbol{\tau}$):

$$\boldsymbol{\tau} = \mathbf{F}\cdot\mathbf{S}\cdot\mathbf{F}^T = \mathbf{F}\cdot\frac{\partial \psi(\mathbf{E})}{\partial \mathbf{E}}\cdot\mathbf{F}^T = 2\mathbf{F}\cdot\frac{\partial \psi(\mathbf{C})}{\partial \mathbf{C}}\cdot\mathbf{F}^T \tag{4.64}$$

- The Cauchy stress tensor ($\boldsymbol{\sigma}$):

$$\begin{aligned} \boldsymbol{\tau} = J\boldsymbol{\sigma} = \mathbf{F}\cdot\mathbf{S}\cdot\mathbf{F}^T &= 2\mathbf{F}\cdot\frac{\partial \psi(\mathbf{C})}{\partial \mathbf{C}}\cdot\mathbf{F}^T \\ \boldsymbol{\sigma} = J\,\mathbf{P}\cdot\mathbf{F}^{-T} &= J\frac{\partial \psi(\mathbf{F})}{\partial \mathbf{F}}\cdot\mathbf{F}^{-T} \end{aligned} \tag{4.65}$$

- The first Piola-Kirchhoff stress tensor ($\mathbf{P}$):

$$\mathbf{P} = \boldsymbol{\tau}\cdot\mathbf{F}^{-T} = \mathbf{F}\cdot\mathbf{S}\cdot\mathbf{F}^T\cdot\mathbf{F}^{-T} = \mathbf{F}\cdot\mathbf{S} = \mathbf{F}\cdot 2\frac{\partial \psi(\mathbf{C})}{\partial \mathbf{C}} \tag{4.66}$$

The rate of change of the constitutive equation 4.63 can be expressed as [18],

$$\dot{\mathbf{S}} = \frac{\partial^2 \psi(\mathbf{E})}{\partial \mathbf{E}\otimes\partial \mathbf{E}}:\dot{\mathbf{E}} = \mathbb{C}^{ton}:\dot{\mathbf{E}} \tag{4.67}$$

where $\mathbb{C}$ is the fourth order tensor known as the material elastic tangent stiffness tensor, also known as the material tangent elasticity tensor. According to the relationship, equation 4.32, of the tensors $\mathbf{E}$ and $\mathbf{C}$ [18],

$$\dot{\mathbf{S}} = 2\frac{\partial^2 \psi(\mathbf{C})}{\partial \mathbf{C}\otimes\partial \mathbf{C}}:\dot{\mathbf{C}} \quad \Rightarrow \quad \dot{\mathbf{S}} = 4\frac{\partial^2 \psi(\mathbf{C})}{\partial \mathbf{C}\otimes\partial \mathbf{C}}:\dot{\mathbf{E}} = \mathbb{C}^{ton}:\dot{\mathbf{E}} \tag{4.68}$$

Then, taking into account equations 4.63, 4.67 and 4.68 it is possible to conclude (in reference configuration) that [18],

$$\mathbb{C}^{ton} = \frac{\partial^2 \psi(\mathbf{E})}{\partial \mathbf{E} \otimes \partial \mathbf{E}} = \frac{\partial \mathbf{S}}{\partial \mathbf{E}} = 4\frac{\partial^2 \psi(\mathbf{C})}{\partial \mathbf{C} \otimes \partial \mathbf{C}} = 2\frac{\partial \mathbf{S}}{\partial \mathbf{C}} \tag{4.69}$$

The tensor $\mathbb{C}^{ton}$ is symmetric and, in the general case, it is anisotropic, having 21 independent components [18].

## 4.12 Isotropic Hyperelastic Materials

For isotropic hyperelastic materials the energy function $\psi(\mathbf{C})$ must satisfy the following condition [18],

$$\psi(\mathbf{C}) = \psi(\mathbf{Q} \cdot \mathbf{C} \cdot \mathbf{Q}^T) \tag{4.70}$$

for any orthogonal tensor $\mathbf{Q}$. Using the polar decomposition and considering the equation 4.24 it is possible to conclude that [18],

$$\psi(\mathbf{C}) = \psi(\mathbf{b}) \tag{4.71}$$

Whence, the energy function, $\psi$, for isotropic materials can be expressed in terms of the left Cauchy-Green deformation tensor [18],

$$\psi(\mathbf{C}, \mathbf{X}) = \psi(\mathbf{b}, \mathbf{x}) \tag{4.72}$$

The scalar-valued isotropic tensor function, $\psi(\mathbf{C})$, can be written in terms of the principal invariants of $\mathbf{C}$ or $\mathbf{b}$ [18],

$$\psi(\mathbf{C}) = \psi(I_{\mathbf{C}}, II_{\mathbf{C}}, III_{\mathbf{C}}) = \psi(I_{\mathbf{b}}, II_{\mathbf{b}}, III_{\mathbf{b}}) \tag{4.73}$$

where $I_{\mathbf{C}}, II_{\mathbf{C}}, III_{\mathbf{C}}$ and $I_{\mathbf{b}}, II_{\mathbf{b}}, III_{\mathbf{b}}$ are the principal invariants of $\mathbf{C}$ and $\mathbf{b}$, respectively. It is important to notice that $\mathbf{C}$ and $\mathbf{b}$ have the same eigenvalues [18].

The constitutive equation in terms of the principal invariants of $\mathbf{C}$ is as follows [18],

$$\mathbf{S} = 2\frac{\partial \psi(\mathbf{C})}{\partial \mathbf{C}} = 2\left[\left(\frac{\partial \psi}{\partial I_{\mathbf{C}}} + \frac{\partial \psi}{\partial II_{\mathbf{C}}} I_{\mathbf{C}}\right)\mathbf{1} - \left(\frac{\partial \psi}{\partial II_{\mathbf{C}}}\right)\mathbf{C} + \left(\frac{\partial \psi}{\partial III_{\mathbf{C}}} III_{\mathbf{C}}\right)\mathbf{C}^{-1}\right] \tag{4.74}$$

Now, considering the relationship between the Kirchhoff stress and the second Piola-Kirchhoff stress tensors, the constitutive equation in the reference configuration, $\mathbf{S} = 2\psi_{\mathbf{C}}$, and the following relationship [18],

$$\psi_{\mathbf{b}} \cdot \mathbf{b} = \mathbf{F} \cdot \psi_{\mathbf{C}} \cdot \mathbf{F}^T = \mathbf{b} \cdot \psi_{\mathbf{b}} \tag{4.75}$$

it is possible to obtain the constitutive equation in the current configuration [18],

$$\boldsymbol{\tau} = \mathbf{F}\cdot\mathbf{S}\cdot\mathbf{F}^T = \mathbf{F}\cdot 2\psi_{\mathbf{C}}\cdot\mathbf{F}^T = 2\psi_{\mathbf{b}}\cdot\mathbf{b} = 2\mathbf{b}\cdot\psi_{\mathbf{b}} \tag{4.76}$$

In similar fashion to equation 4.74 [18],

$$\boldsymbol{\tau} = J\boldsymbol{\sigma} = 2\mathbf{F}\cdot\left[\left(\frac{\partial\psi}{\partial I_{\mathbf{C}}} + \frac{\partial\psi}{II_{\mathbf{C}}}I_{\mathbf{C}}\right)\mathbf{1} - \frac{\partial\psi}{\partial II_{\mathbf{C}}}\mathbf{C} + \frac{\partial\psi}{\partial III_{\mathbf{C}}}III_{\mathbf{C}}\mathbf{C}^{-1}\right]\cdot\mathbf{F}^T \tag{4.77}$$

Considering $\mathbf{C} = \mathbf{F}^T\cdot\mathbf{F}$ and $\mathbf{b} = \mathbf{F}\cdot\mathbf{F}^T$, the above equation becomes [18],

$$\boldsymbol{\tau} = J\boldsymbol{\sigma} = 2\left[\left(\frac{\partial\psi}{\partial I_{\mathbf{b}}} + \frac{\partial\psi}{II_{\mathbf{b}}}I_{\mathbf{b}}\right)\mathbf{b} - \frac{\partial\psi}{\partial II_{\mathbf{b}}}\mathbf{b}^2 + \frac{\partial\psi}{\partial III_{\mathbf{b}}}III_{\mathbf{b}}\mathbf{1}\right] \tag{4.78}$$

Additionally, one can represent equation 4.78 in a different way, by substituting the expression $\mathbf{b}^2$ by means of the Cayley-Hamilton theorem [18],

$$\boldsymbol{\tau} = J\boldsymbol{\sigma} = 2\left[\left(\frac{\partial\psi}{\partial III_{\mathbf{b}}}III_{\mathbf{b}} + \frac{\partial\psi}{II_{\mathbf{b}}}II_{\mathbf{b}}\right)\mathbf{1} + \left(\frac{\partial\psi}{\partial I_{\mathbf{b}}}\right)\mathbf{b} + \left(\frac{\partial\psi}{\partial II_{\mathbf{b}}}III_{\mathbf{b}}\right)\mathbf{b}^{-1}\right] \tag{4.79}$$

The strain energy function can also be expressed in terms of the principal stretches, $\lambda_i$ (with $i = 1,2,3$) [18],

$$\psi = \psi(\lambda_1,\lambda_2,\lambda_3) \tag{4.80}$$

In this case, the second Piola-Kirchhoff stress tensor, $\mathbf{S}$, becomes [18],

$$\mathbf{S} = 2\frac{\partial\psi(\mathbf{C})}{\partial\mathbf{C}} = 2\frac{\partial\psi}{\partial\lambda_i}\frac{\partial\lambda_i}{\partial\mathbf{C}} = 2\left(\frac{\partial\psi}{\partial\lambda_1}\frac{\partial\lambda_1}{\partial\mathbf{C}} + \frac{\partial\psi}{\partial\lambda_2}\frac{\partial\lambda_2}{\partial\mathbf{C}} + \frac{\partial\psi}{\partial\lambda_3}\frac{\partial\lambda_3}{\partial\mathbf{C}}\right) \tag{4.81}$$

$$\mathbf{S} = \sum_{i=1}^{3}\frac{1}{\lambda_i}\frac{\partial\psi}{\partial\lambda_i}\mathbf{N}^i\otimes\mathbf{N}^i = \sum_{i=1}^{3}S_i\mathbf{N}^i\otimes\mathbf{N}^i \tag{4.82}$$

As regards the Cauchy stress tensor [18],

$$\boldsymbol{\sigma} = J^{-1}\mathbf{F}\cdot\mathbf{S}\cdot\mathbf{F}^T = \sum_{i=1}^{3}J^{-1}\frac{1}{\lambda_i}\frac{\partial\psi}{\partial\lambda_i}\left(\mathbf{F}\cdot\mathbf{N}^i\otimes\mathbf{F}\cdot\mathbf{N}^i\right) \tag{4.83}$$

## 4.13 Incompressible Materials

Many materials are considered to be incompressible, as they can be subjected to large deformations without any volume change being observed. In these situations, the continuum is characterized by isochoric motion [18],

$$\det(\mathbf{F}) = J = \lambda_1\lambda_2\lambda_3 = 1 \tag{4.84}$$

It is important to enhance that in imcompressible materials the stress state is not completely determined by the strain rate, since in an incompressible body hydrostatic stress can be added

to the current stress state without changing the strain rate. Moreover, in isotropic materials, a hydrostatic state produces only volumetric deformations which makes the volumetric deformation in incompressible materials equal to zero for any hydrostatic state. Here, energy is not also affected by the volumetric part ($\psi(\mathbf{F}^{vol}) = \psi(\mathbf{1}) = 0$) [18].

The hydrostatic stress state is expressed as [18],

$$\boldsymbol{\sigma}^{hyd} = -p\mathbf{1} \tag{4.85}$$

where $p$ denotes pressure.

By taking the relationship between the Cauchy stress and the second Piola-Kirchhoff stress tensors, the volumetric part of $\mathbf{S}$ can be obtained [18],

$$\mathbf{S}^{hyd} = -Jp\mathbf{C}^{-1} \tag{4.86}$$

thus,

$$\mathbf{S} = 2\frac{\partial \psi(\mathbf{C})}{\partial \mathbf{C}} - Jp\mathbf{C}^{-1} \tag{4.87}$$

In order to solve a problem with the constraint $J = 1$, the Lagrange multiplier, $\gamma$, can be introduced. It must satisfy the following [18],

$$\psi = \psi(\mathbf{C}) + \gamma(J-1) \tag{4.88}$$

By taking the derivative of the equation 4.88 with respect to $\mathbf{C}$, the second Piola-Kirchhoff stress tensor can be obtained [18],

$$\mathbf{S} = 2\frac{\partial \psi(\mathbf{C})}{\partial \mathbf{C}} + J\gamma\mathbf{C}^{-1} \tag{4.89}$$

Therefore,

$$\gamma = -p \tag{4.90}$$

Finally, the constitutive equation for the first Piola-Kirchhoff stress tensor and for the Cauchy stress tensor is given, respectively, by [18],

$$\mathbf{P} = \frac{\partial \psi(\mathbf{F})}{\partial \mathbf{F}} - p\mathbf{F}^{-T} \tag{4.91}$$

$$\boldsymbol{\sigma} = \frac{\partial \psi(\mathbf{F})}{\partial \mathbf{F}} \cdot \mathbf{F}^T - p\mathbf{1} = \mathbf{F} \cdot \left(\frac{\partial \psi(\mathbf{F})}{\partial \mathbf{F}}\right)^T - p\mathbf{1} \tag{4.92}$$

## 4.14 Compressible Materials

In compressible hyperelastic materials, unlike incompressible materials, they go through a change in volume during the deformation process. Thus, it would be appropriate to separate the motion undergone intro isochoric motion and another type characterized by dilatational transformation (purely volume change). Thereby, a multiplicative decomposition of the deformation gradient can be considered as follows [18],

$$\mathbf{F} = \widetilde{\mathbf{F}} \cdot \mathbf{F}^{vol} \tag{4.93}$$

where $\widetilde{\mathbf{F}}$ is the isochoric transformation and $\mathbf{F}^{vol}$ is the dilatational transformation [18].

Considering $\mathbf{F}$, $\mathbf{C}$ and $\mathbf{b}$ it is possible to write [18],

$$\begin{aligned} \widetilde{\mathbf{F}} &= J^{-\frac{1}{3}}\mathbf{F} \quad ; \quad \mathbf{F}^{vol} = J^{\frac{1}{3}}\mathbf{1} \\ \widetilde{\mathbf{C}} &= J^{-\frac{2}{3}}\mathbf{C} \quad ; \quad \mathbf{C}^{vol} = J^{\frac{2}{3}}\mathbf{1} \\ \widetilde{\mathbf{b}} &= J^{-\frac{2}{3}}\mathbf{b} \quad ; \quad \mathbf{b}^{vol} = J^{\frac{2}{3}}\mathbf{1} \end{aligned} \tag{4.94}$$

and,

$$\widetilde{J} = |\widetilde{\mathbf{F}}| = |J^{-\frac{1}{3}}\mathbf{F}| = 1 \quad ; \quad J^{vol} = |\mathbf{F}^{vol}| = |J^{\frac{1}{3}}\mathbf{1}| = J \tag{4.95}$$

After some manipulation, a new fourth order tensor, with respect to the reference configuration, can be introduced. It is known as the projection tensor, $\mathbb{P}$ [18],

$$\mathbb{P} = \mathbf{II} - \frac{1}{3}\mathbf{C} \otimes \mathbf{C}^{-1} \tag{4.96}$$

where $\mathbf{II}$ is the fourth order unit tensor [18].

A stress tensor can also be defined, analogous to the Cauchy stress tensor, in the intermediate configuration by means of the transformation $\mathbf{F}^{vol}$, which leads to [18],

$$\overline{\boldsymbol{\sigma}}^{vol} = \frac{\partial \psi(J)}{\partial J}\mathbf{1} \tag{4.97}$$

It is also possible to define a stress tensor in the intermediate configuration caused by the transformation $\widetilde{\mathbf{F}}$ [18],

$$\widetilde{\overline{\boldsymbol{\sigma}}} = 2\frac{\partial \widetilde{\psi}(\widetilde{\mathbf{C}})}{\partial \widetilde{\mathbf{C}}} \tag{4.98}$$

Additive decomposition can be used in strain energy function in order to isolate the isochoric and volumetric components [18],

$$\begin{aligned} \psi(\mathbf{F}) &= \widetilde{\psi}(\widetilde{\mathbf{F}}) + \psi^{vol}(\mathbf{F}^{vol}) \\ \psi(\mathbf{C}) &= \widetilde{\psi}(\widetilde{\mathbf{C}}) + \psi^{vol}(\mathbf{C}^{vol}) \end{aligned} \tag{4.99}$$

Using the chain rule of derivative of the strain energy function, knowing that the relationship $\dot{J} = \frac{J}{2}\mathbf{C}^{-1}{:}\dot{\mathbf{C}}$ can be obtained and that the term $\dot{\widetilde{\mathbf{C}}}$ can be expressed as $\dot{\widetilde{\mathbf{C}}} = \frac{\partial \widetilde{\mathbf{C}}}{\partial \mathbf{C}}{:}\dot{\mathbf{C}} = J^{-\frac{2}{3}}\mathbb{P}^T{:}\dot{\mathbf{C}}$ [18],

$$\begin{aligned}\dot{\psi}(\mathbf{C}) &= J^{-\frac{2}{3}}\frac{\partial \widetilde{\psi}(\widetilde{\mathbf{C}})}{\partial \widetilde{\mathbf{C}}}{:}\mathbb{P}^T{:}\dot{\mathbf{C}} + \frac{J}{2}\frac{d\psi^{vol}(J)}{dJ}\mathbf{C}^{-1}{:}\dot{\mathbf{C}} \\ &= J^{-\frac{2}{3}}\mathbb{P}{:}\frac{\partial \widetilde{\psi}(\widetilde{\mathbf{C}})}{\partial \widetilde{\mathbf{C}}}{:}\dot{\mathbf{C}} + \frac{J}{2}\frac{d\psi^{vol}(J)}{dJ}\mathbf{C}^{-1}{:}\dot{\mathbf{C}}\end{aligned} \tag{4.100}$$

Regarding the equation 4.100 and that in purely elastic materials the internal energy dissipation is zero [18],

$$\mathbf{S} = 2J^{-\frac{2}{3}}\mathbb{P}{:}\frac{\partial \widetilde{\psi}(\widetilde{\mathbf{C}})}{\partial \widetilde{\mathbf{C}}} + J\frac{d\psi^{vol}(J)}{dJ}\mathbf{C}^{-1} \tag{4.101}$$

Finally, taking the definition of the tensor $\mathbf{S}$ and the definition of the energy function in equation 4.99 [18],

$$\mathbf{S} = 2\frac{\partial \psi(\mathbf{C})}{\partial \mathbf{C}} = 2\frac{\partial}{\partial \mathbf{C}}\left[\widetilde{\psi}(\widetilde{\mathbf{C}}) + \psi^{vol}(\mathbf{C}^{vol})\right] = 2\frac{\partial \widetilde{\psi}(\widetilde{\mathbf{C}})}{\partial \mathbf{C}} + 2\frac{\partial \psi^{vol}(\mathbf{C}^{vol})}{\partial \mathbf{C}} = \widetilde{\mathbf{S}} + \mathbf{S}^{vol} \tag{4.102}$$

where,

$$\mathbf{S}^{vol} = 2\frac{\partial \psi^{vol}(\mathbf{C}^{vol})}{\partial \mathbf{C}} = 2\frac{\partial \psi^{vol}(J)}{\partial J}\frac{\partial J}{\partial \mathbf{C}} = 2\frac{\partial \psi^{vol}(J)}{\partial J}\frac{1}{2}J\mathbf{C}^{-1} = J\frac{\partial \psi^{vol}(J)}{\partial J}\mathbf{C}^{-1} \tag{4.103}$$

$$\widetilde{\mathbf{S}} = 2\frac{\partial \widetilde{\psi}(\widetilde{\mathbf{C}})}{\partial \mathbf{C}} = 2\frac{\partial \widetilde{\psi}(\widetilde{\mathbf{C}})}{\partial \widetilde{\mathbf{C}}}{:}\frac{\partial \widetilde{\mathbf{C}}}{\partial \mathbf{C}} = J^{-\frac{2}{3}}\mathbb{P}{:}\left(2\frac{\partial \widetilde{\psi}(\widetilde{\mathbf{C}})}{\partial \widetilde{\mathbf{C}}}\right) = J^{-\frac{2}{3}}\mathbb{P}{:}\widetilde{\overline{\mathbf{S}}} \tag{4.104}$$

In the specific case when materials are considered to be compressible and isotropic, the energy function decomposition can be given by [18],

$$\psi(\mathbf{C}) = \psi(\mathbf{b}) = \widetilde{\psi}(\widetilde{\mathbf{b}}) + \psi^{vol}(J) \tag{4.105}$$

and the stress equation [18],

$$\begin{aligned}\boldsymbol{\sigma} &= J^{-1}2\frac{\partial \psi(\mathbf{b})}{\partial \mathbf{b}}\cdot\mathbf{b} = J^{-1}2\frac{\partial}{\partial \mathbf{b}}\left[\widetilde{\psi}(\widetilde{\mathbf{b}}) + \psi^{vol}(J)\right]\cdot\mathbf{b} = \\ &= J^{-1}2\frac{\partial \widetilde{\psi}(\widetilde{\mathbf{b}})}{\partial \mathbf{b}}\cdot\mathbf{b} + J^{-1}2\frac{\partial \psi^{vol}(J)}{\partial \mathbf{b}}\cdot\mathbf{b} = \widetilde{\boldsymbol{\sigma}} + \boldsymbol{\sigma}^{vol}\end{aligned} \tag{4.106}$$

where,

$$\begin{aligned}\boldsymbol{\sigma}^{vol} &= J^{-1}2\frac{\partial \psi^{vol}(J)}{\partial \mathbf{b}}\cdot\mathbf{b} = J^{-1}2\frac{\partial \psi^{vol}(J)}{\partial J}\frac{\partial J}{\partial \mathbf{b}}\cdot\mathbf{b} = \\ &= J^{-1}2\frac{\partial \psi^{vol}(J)}{\partial J}\frac{J}{2}\mathbf{b}^{-1}\cdot\mathbf{b} = \frac{\partial \psi^{vol}(J)}{\partial J}\mathbf{1}\end{aligned} \tag{4.107}$$

$$\begin{aligned}\widetilde{\boldsymbol{\sigma}} = J^{-1}2\mathbf{b}\cdot\frac{\partial\widetilde{\psi}(\widetilde{\mathbf{b}})}{\partial\mathbf{b}} = J^{-1}2\mathbf{b}\cdot J^{-\frac{2}{3}}\left(\mathbf{II}-\frac{1}{3}\mathbf{b}^{-1}\otimes\mathbf{b}\right):\frac{\partial\widetilde{\psi}(\widetilde{\mathbf{b}})}{\partial\widetilde{\mathbf{b}}} = \\ = \mathbf{b}\cdot\left(J^{-\frac{2}{3}}\mathbf{II}-\frac{1}{3}\mathbf{b}^{-1}\otimes\widetilde{\mathbf{b}}\right)\cdot\widetilde{\mathbf{b}}^{-1}:2J^{-1}\frac{\partial\widetilde{\psi}(\widetilde{\mathbf{b}})}{\partial\widetilde{\mathbf{b}}}\cdot\widetilde{\mathbf{b}}\end{aligned} \tag{4.108}$$

## 4.15 Anisotropic Hyperelasticity

Some materials, such as biological tissues, have fibers and, therefore lose their isotropy. When they are arranged according to a preferential direction it is possible to approach the material by means of the transversely isotropic material [18].

As stated previously, the scalar valued tensor function, $\psi$, can be written in terms of the principal invariants of $\mathbf{C}$. In this particular case, the fibers preferential direction, $\mathbf{a}_0$, is also an argument of the function. It can be shown that this function can be written in terms of the following invariants [18],

$$\psi(\mathbf{C},\mathbf{a}_0) = \psi(I_\mathbf{C},II_\mathbf{C},III_\mathbf{C},\mathbf{a}_0\cdot\mathbf{C}\cdot\mathbf{a}_0,\mathbf{a}_0\cdot\mathbf{C}^2\cdot\mathbf{a}_0) = \psi(I_\mathbf{C},II_\mathbf{C},III_\mathbf{C},I_\mathbf{C}^{(4)},I_\mathbf{C}^{(5)}) \tag{4.109}$$

where $I_\mathbf{C}^{(4)}$ and $I_\mathbf{C}^{(5)}$ are the pseudo-invariants of anisotropy. Moreover, if the energy is considered to be independent of the sense of the vector $\mathbf{a}_0$, the strain energy function can be represented by [18],

$$\psi = \psi(\mathbf{C},\mathbf{a}_0\otimes\mathbf{a}_0) \tag{4.110}$$

As the material is no longer isotropic, it is not possible to express the energy function just in terms of the principal invariants. To use this definition, two pseudo-invariants of anisotropy were obtained by Spencer (1984), which contribute to the energy function and are defined as [18],

$$\begin{aligned}I_\mathbf{C}^{(4)} &= \mathbf{a}_0\cdot\mathbf{C}\cdot\mathbf{a}_0 \\ I_\mathbf{C}^{(5)} &= \mathbf{a}_0\cdot\mathbf{C}^2\cdot\mathbf{a}_0\end{aligned} \tag{4.111}$$

where $I_\mathbf{C}^{(4)} = \lambda_{\mathbf{a}_0}^2$ and $\lambda_{\mathbf{a}_0}$ is the stretch according to the direction $\mathbf{a}_0$ [18].

The constitutive equation for stress, in reference configuration, can be expressed by [18],

$$\begin{aligned}\mathbf{S} = 2\frac{\partial\psi(I_\mathbf{C},II_\mathbf{C},III_\mathbf{C},I_\mathbf{C}^{(4)},I_\mathbf{C}^{5})}{\partial\mathbf{C}} = \\ = 2\left(\frac{\partial\psi}{\partial I_\mathbf{C}}\frac{I_\mathbf{C}}{\partial\mathbf{C}}+\frac{\partial\psi}{\partial II_\mathbf{C}}\frac{II_\mathbf{C}}{\partial\mathbf{C}}+\frac{\partial\psi}{\partial III_\mathbf{C}}\frac{III_\mathbf{C}}{\partial\mathbf{C}}+\frac{\partial\psi}{\partial I_\mathbf{C}^{(4)}}\frac{I_\mathbf{C}^{(4)}}{\partial\mathbf{C}}+\frac{\partial\psi}{\partial I_\mathbf{C}^{(5)}}\frac{I_\mathbf{C}^{(5)}}{\partial\mathbf{C}}\right)\end{aligned} \tag{4.112}$$

Considering the derivatives of $I_{\mathbf{C}}^{(4)}$ and $I_{\mathbf{C}}^{(5)}$ with respect to the tensor $\mathbf{C}$ and the equation 4.74 [18],

$$\begin{aligned}\mathbf{S} = 2\left[\left(\frac{\partial \psi}{\partial I_{\mathbf{C}}}\right)\mathbf{1} + \left(\frac{\partial \psi}{\partial II_{\mathbf{C}}} II_{\mathbf{C}} + \frac{\partial \psi}{\partial III_{\mathbf{C}}} III_{\mathbf{C}}\right)\mathbf{C}^{-1} - \left(\frac{\partial \psi}{\partial II_{\mathbf{C}}} III_{\mathbf{C}}\right)\mathbf{C}^{-2}\right. \\ \left. + \frac{\partial \psi}{\partial I_{\mathbf{C}}^{(4)}}\mathbf{a}_0 \otimes \mathbf{a}_0 + \frac{\partial \psi}{\partial I_{\mathbf{C}}^{(5)}}\left(\mathbf{a}_0 \otimes (\mathbf{C}\cdot\mathbf{a}_0) + (\mathbf{a}_0 \cdot \mathbf{C}) \otimes \mathbf{a}_0\right)\right]\end{aligned} \tag{4.113}$$

Using the expression of the Kirchhoff stress tensor and considering the direction of the fibers in the current configuration, $\mathbf{a}_0$ [18],

$$\begin{aligned}\boldsymbol{\tau} = J\,\sigma = \mathbf{F}\cdot\mathbf{S}\cdot\mathbf{F}^T \\ = 2\mathbf{F}\cdot\left[\left(\frac{\partial \psi}{\partial I_{\mathbf{C}}}\right)\mathbf{1} + \left(\frac{\partial \psi}{\partial II_{\mathbf{C}}} II_{\mathbf{C}} + \frac{\partial \psi}{\partial III_{\mathbf{C}}} III_{\mathbf{C}}\right)\mathbf{C}^{-1} - \left(\frac{\partial \psi}{\partial II_{\mathbf{C}}} III_{\mathbf{C}}\right)\mathbf{C}^{-2}\right. \\ \left. + \frac{\partial \psi}{\partial I_{\mathbf{C}}^{(4)}}\mathbf{a}_0 \otimes \mathbf{a}_0 + \frac{\partial \psi}{\partial I_{\mathbf{C}}^{(5)}}\left(\mathbf{a}_0 \otimes (\mathbf{C}\cdot\mathbf{a}_0) + (\mathbf{a}_0 \cdot \mathbf{C}) \otimes \mathbf{a}_0\right)\right]\cdot\mathbf{F}^T\end{aligned} \tag{4.114}$$

## 4.16 Hyperelastic Models

Over the years, several models have been developed in order to simulate the phenomenological behavior of hyperelastic materials. There are some models that do not account for the anisotropy of the materials (the Neo-Hookean, Ogden, Mooney-Rivlin, Yeoh material models, for example) and others that take it into consideration (the Holzapfel-Gasser-Ogden and Martins material models, for example) [18].

The strain energy functions for those material models are as follows,

- The Neo-Hookean Material Model [19]

$$\psi = \frac{\mu}{2}(\bar{I}_{\mathbf{C}} - 3) + \frac{K_0}{2}\left(J^{el} - 1\right)^2 = c_1(\bar{I}_{\mathbf{C}} - 3) + \frac{1}{D_1}\left(J^{el} - 1\right)^2 \tag{4.115}$$

  where $\psi$ is the strain energy function per unit of volume, $\mu$ and $K_0$ are known as the shear and bulk modulus, respectively, $C_1$ and $D_1$ are temperature-dependent material parameters and $\bar{I}_{\mathbf{C}}$ is the first deviatoric strain invariant, which is defined as $\bar{I}_{\mathbf{C}} = \bar{\lambda_1}^2 + \bar{\lambda_2}^2 + \bar{\lambda_3}^2$. $\bar{\lambda_i}$ are the principal stretches and are given by $\bar{\lambda_i} = J^{-\frac{1}{3}}\lambda_i$ (where $J$ is the total volume ratio) and $J^{el}$ is the elastic volume ratio.

- The Ogden Material Model (in terms of the principal stretches) [19]

$$\psi = \sum_{p=1}^{N}\frac{2\mu_p}{\alpha_p^2}(\bar{\lambda_1}^{\alpha_p} + \bar{\lambda_2}^{\alpha_p} + \bar{\lambda_3}^{\alpha_p} - 3) + \sum_{p=1}^{N}\frac{1}{D_p}\left(J^{el} - 1\right)^{2p} \tag{4.116}$$

  where $N, \mu_p, \alpha_p$ are the material constants.

- The Mooney-Rivlin Material Model [19]

$$\psi = c_1(\bar{I}_{\mathbf{C}} - 3) + c_2(\bar{II}_{\mathbf{C}} - 3) + \frac{1}{D_1}\left(J^{el} - 1\right)^2 \tag{4.117}$$

where $\bar{II}_{\mathbf{C}} = \bar{\lambda_1}^{-2} + \bar{\lambda_2}^{-2} + \bar{\lambda_3}^{-2}$ and it is the second deviatoric strain invariant.

- The Yeoh Material Model [19]

$$\begin{gathered}\psi = c_1(\bar{I}_{\mathbf{C}} - 3) + c_2(\bar{I}_{\mathbf{C}} - 3)^2 + c_3(\bar{I}_{\mathbf{C}} - 3)^3 + \\ \frac{1}{D_1}\left(J^{el} - 1\right)^2 + \frac{1}{D_2}\left(J^{el} - 1\right)^4 + \frac{1}{D_3}\left(J^{el} - 1\right)^6\end{gathered} \tag{4.118}$$

where $c_1, c_2$ and $c_3$ are material constants.

- The Holzapfel-Gasser-Ogden Material Model [19]

$$\psi = c_1(\bar{I}_{\mathbf{C}} - 3) + \frac{1}{D}\left(\frac{\left(J^{el}\right)^2 - 1}{2} - \ln J^{el}\right) + \frac{k_1}{2k_2}\sum_{\alpha=1}^{N}\left(\mathrm{e}^{k_2\bar{E}_\alpha^2} - 1\right) \tag{4.119}$$

with $\bar{E}_\alpha = \kappa(\bar{I}_{\mathbf{C}} - 3) + (1 - 3\kappa)(\bar{I}^{(4)}_{\mathbf{C}\alpha\alpha} - 1)$, where $c_1, D, k_1, k_2$ and $\kappa$ are temperature-dependent material parameters, $N$ is the number of families of fibers ($N \leq 3$) and $\psi$ is the strain energy per unit of reference volume. $J^{el}$ is the elastic volume ratio and the parameter $\kappa (0 \leq \kappa \leq \frac{1}{3})$ describes the level of dispersion in fiber directions. When $\kappa = \frac{1}{3}$, the fibers are randomly distributed and the material becomes isotropic. On the other hand, when $\kappa = 0$, the fibers are perfectly aligned.

- The Martins Material model (modified form of the incompressible transversely isotropic hyperelastic model proposed by Humphrey and Yin) [20], [21]

$$\begin{gathered}\psi = \psi_I + \psi_{pass} + \psi_{act} + \psi_J \\ \psi_J = \frac{1}{D}(J-1)^2 \\ \psi_I = c\left(\mathrm{e}^{b(\bar{I}_{\mathbf{C}}-3)} - 1\right) \\ \psi_{pass} = A\left(\mathrm{e}^{a(\bar{\lambda}_f - 1)^2} - 1\right) \\ \psi_{act} = T_0^M \int_1^{\bar{\lambda}_f} f_{SE}\left(\lambda^M, \alpha\right) d\lambda^M \\ f_{SE} = \alpha \begin{cases} 1 - 4\left(\lambda^M - 1\right)^2 & 0.5 < \lambda^M < 1.5, \\ 0 & \text{otherwise} \end{cases}\end{gathered} \tag{4.120}$$

where $\psi$ is the strain energy function per unit of volume, $\psi_J$ is the strain energy term associated with the volume change, $\psi_I$ is the strain energy stored in the material, $\psi_{pass}$ is the strain energy term related to the passive part of the fiber and $\psi_{act}$ is the active part of the

fiber. $\bar{\lambda}_f$ is the stretch ratio that is observed in the fiber direction of the undeformed fiber and $b$ and $a$ are material constants with no physical dimensions. On the other hand, $c$ and $A$ have pressure dimensions. $\bar{I}_{\mathbf{C}}$ represents the first invariant of the right Cauchy-Green strain tensor with the volume change eliminated.

## 4.17 Viscoelasticity

Every material exhibit some viscoelastic response. Although the behavior of some materials, subjected to specific conditions (temperature and small deformations), do not deviate much from linear elasticity, there are others which viscoelastic effects are significant. Synthetic polymers, wood, human tissue as well as metals at high temperature are some of these examples [22].

A material that is classified as viscoelastic combines characteristics of elastic and viscous behavior [23]. In viscoelastic materials the relationship between stress and strain depends on time. There are some typical phenomena concerning viscoelastic materials [22]:

- Creep;
- Relaxation;
- Hysteresis;
- The rate of application of the load influences the effective stiffness;
- Acoustic waves experience attenuation;
- Rebound of an object following an impact is less than 100%;
- There is frictional resistance during rolling.

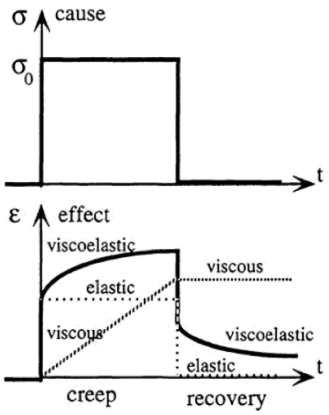


Figure 4.4: Creep phenomenon and recovery [22].

As far as creep is concerned, it is a slow and progressive phenomenon in which a material is subjected to constant stress. As it is possible to observe in figure 4.4, once the load is applied

the material deforms until it is released. At this point, the material recovers in terms of strain. Depending on the material, the strain recovery may or may not approach zero, which differs from elastic materials that exhibit immediate recovery to zero strain, since the energy used to deform it is stored in it as potential energy [22].

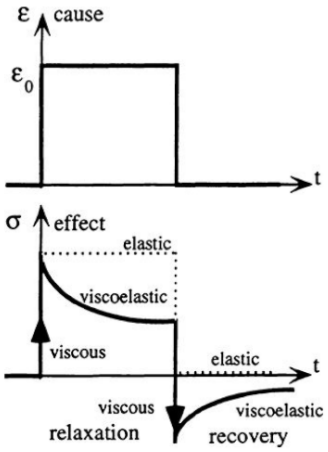


Figure 4.5: Relaxation phenomenon and recovery [22].

The phenomenon in which the stress gradually decreases when the material is held at constant strain is known as relaxation. Its typical behavior is shown in figure 4.5. In order to characterize the viscoelastic behavior of a material, stress relaxation testing is used. The material is loaded to a predifined strain and it is held there for a period of time, while it is recorded the change of load required to hold it [22].

Finally, when cyclic loading is applied, another typical phenomenon concerning viscoelastic materials can be verified - hysteresis. The typical behavior in this case in shown in figure 4.6. The area enclosed by the loading and unloading paths is called hysteresis loop, which represents the energy dissipated as heat during the deformation and recovery states [22].

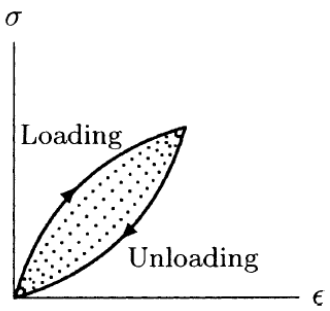


Figure 4.6: Hysteresis phenomenon [24].

### 4.17.1 Empirical Models of Viscoelasticity

In viscoelasticity analyses, springs and dashpots are used within the building blocks of a model. Connecting them in various forms lead to the construction of empirical viscoelastic models. As it may be intuitive, springs take into account the elastic solid behavior, while dashpots describe the viscous fluid behavior [24].

An easy way of obtaining a simple empirical model is to connect a spring and a dashpot together in parallel and in series configurations. With regard to the first configuration, figure 4.7, it is known as the Kelvin-Voight model. The latter, is also a well known viscoelastic model, denoted by Maxwell model, figure 4.8 [24].

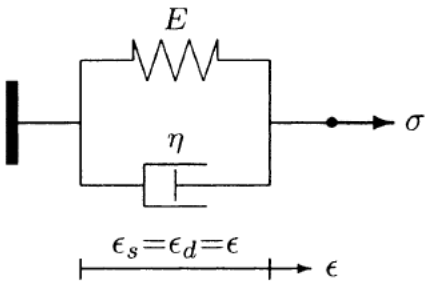


Figure 4.7: Kelvin-Voight model [24].

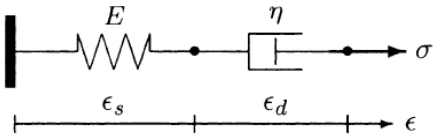


Figure 4.8: Maxwell model [24].

## 4.18 Finite Element Method

Physics laws can describe virtually every phenomonon in nature, whether biological, geological or mechanical, in terms of algebraic, differential or integral equations relating various quantities of interest [25].

Studying physical phenomena involves essentially two major tasks: mathematical formulation of the physical process and numerical analysis of the latter [25].

While the mathematical formulation of a physical process requires background in related subjects and, most often, certain mathematical tools (which often leads to differential equations), in the numerical simulation a numerical method and a computer are needed to evaluate the mathematical model and estimate the characteristics of the process [25].

Obtaining the solution by exact methods of analysis is a very difficult task and for this reason approximate methods of analysis provide alternative means of finding solutions. The finite difference method and variational methods such as the Rayleigh-Ritz and Galerkin methods are the most frequently approximate methods used in the literature. However, the variational methods have a disadvantage – the approximation functions for problems with arbitrary domains are difficult to formulate. The finite element method (FEM) overcomes this problem as it provides a systematic procedure for the derivation of the aprroximation functions over subregions of the domain. This method is endowed with three basic features that account for its superiority over other methods and makes it the most widely applied numerical method. Firstly, a geometrically complex domain of the problem is represented as a collection of geometrically simple subdomains, known as finite elements. Secondly, over each finite element, the approximation functions are derived using the basic idea that any continuous function can de represented by a linear combination of algebraic polynomials, and finally, algebraic relations among the undetermined coefficients (nodal values) are obtained by satisfying the governing equations, often in a weighted integral sense, over each element [25].

Thus, it is possible to build a spatial model of the problem through a discretization process, defining a continuum body into simpler geometrical shapes (finite elements). For this purpose, it is imperative to know the designated weak form of the problem. The latter is established through the designated strong form (differential equation) or, mostly, through the variational principles (i.e. virtual work principle, minimum total potential energy principle). The behavior of each one of these elements is expressed in terms of a finite number of degrees of freedom characterised by the value of determinate functions in a set of nodal points [25].

### 4.18.1 Discretized Equilibrium Equations

The virtual work principle is defined as the work done by all the forces acting on a system during a virtual displacement. It states that the total work done by those forces is zero and it can be presented in its simplest form as,

$$\delta W^e + \delta W^i + \delta W^j = 0 \tag{4.121}$$

where the first term represents the work done by external forces, the second term the work done by internal forces and the third term the work done by inertia forces.

After working on equation 4.121 it is possible to obtain [26],

$$\int\int\int_V \delta\boldsymbol{\varepsilon}^T\boldsymbol{\sigma}\, dV = \int\int\int_V \delta\mathbf{u}^T\mathbf{b}\, dV + \int\int_A \delta\mathbf{u}^T\mathbf{t}\, dA + \sum_i \delta\mathbf{a}_i^T\mathbf{p}_i \tag{4.122}$$

where the first term represents the strain energy storaged within the body, the second term the work done by the body forces, the third term the work done by the forces applied in the boundary surface and the fourth term the work done by the loads acting on the node $i$ [26].

The displacement field can be approximated by interpolation functions, commonly designated by shape functions. Within the finite element the displacement field is obtained by [26],

$$\mathbf{u} = \mathbf{N}\mathbf{a}^{(e)} \tag{4.123}$$

where $\mathbf{N}$ is the shape function of the element and $\mathbf{a}^{(e)}$ is the nodal displacement vector of the element. Interpolating the virtual displacements and the virtual strains in terms of nodal values [26],

$$\begin{aligned} \delta\mathbf{u} &= \mathbf{N}\delta\mathbf{a}^{(e)} \\ \delta\varepsilon &= \mathbf{B}\delta\mathbf{a}^{(e)} \end{aligned} \tag{4.124}$$

and recalling the virtual work expression 4.122, rewriting it in terms of the virtual displacement and after the simplification of the virtual displacements [26],

$$\begin{gathered} \left(\int\int\int_{V^{(e)}} \mathbf{B}^T\mathbf{D}\mathbf{B}\, dV\right)\mathbf{a}^{(e)} - \int\int\int_{V^{(e)}} \mathbf{N}^T\mathbf{b}\, dV - \int\int_{A^{(e)}} \mathbf{N}^T\mathbf{t}\, dA = \mathbf{q}^{(e)} \\ \mathbf{K}^{(e)}\mathbf{a}^{(e)} - \mathbf{f}^{(e)} = \mathbf{q}^{(e)} \end{gathered} \tag{4.125}$$

where $\mathbf{K}^{(e)}$ is the element stiffness matrix, $\mathbf{f}^{(e)}$ is the equivalent nodal force vector for the element and $\mathbf{q}^{(e)}$ is the equilibrating nodal force vector [26].

# Chapter 5

# Simulation

In order to accomplish the purpose of this thesis, firstly, the characterization of the bladder's wall behavior was carried out. To do so, data from the literature, related to uniaxial tensile tests performed with porcine specimens, was taken into account.

The outcome of the work done by Jokandan, Ajalloueian et al., 2017 [27], figure 5.1, exhibits a curious fact - the bladder wall only shows a different behavior when subjected to displacement along circumferential and longitudinal directions, when strain above 200% occurs. Thus, when strain above this value is observed the outer and inner layers of the bladder's wall (which fibers are alligned in a longitudinal direction, as stated before) seem to be stiffer than the middle layer (which has fibers alligned in a circumferential direction). Until this value of strain, the bladder's wall behaves isotropically.

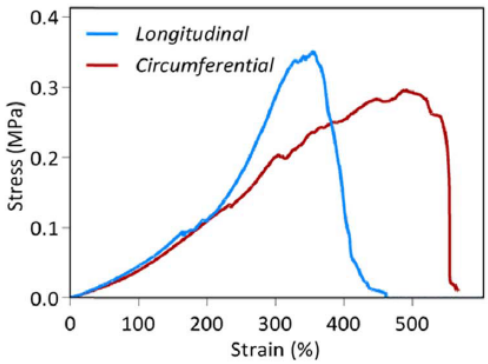


Figure 5.1: Uniaxial tensile test in longitudinal and circumferential directions of porcine bladder [27].

Knowing the maximum strain a bladder is subjected when performing under normal conditions can be useful to determine the region of the curve we are working and decide about the constitutive law to use.

Hence, an approximation of the bladder geometry was made - it was considered to have an ellipsoid shape, figure 5.2, which characteristic dimensions were obtained by an available 3D

model of the bladder. They are shown in table 5.1.

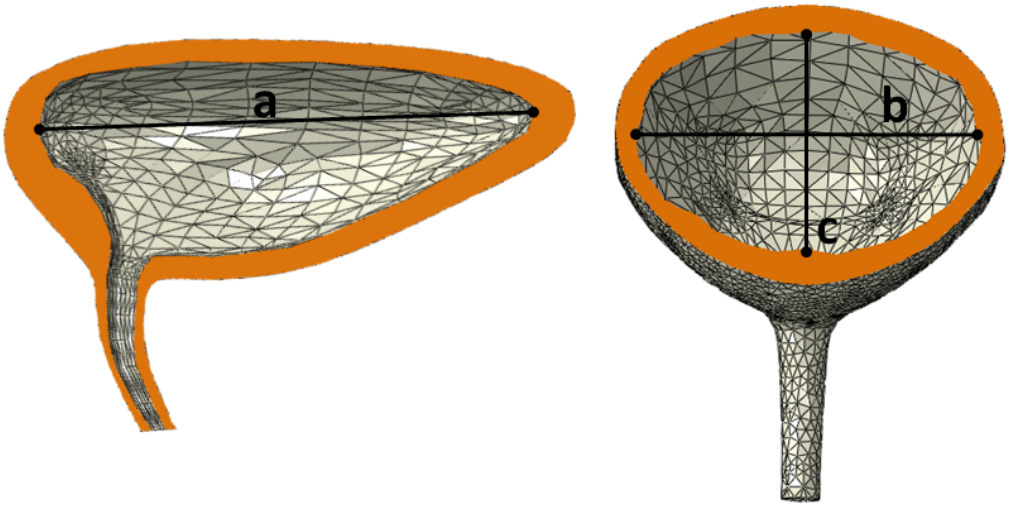


Figure 5.2: Ellipsoid characteristic dimensions.

Table 5.1: Ellipsoid dimensions.

| **Variable** | **Value (cm)** |
|---|---|
| 2a | 7.2 |
| 2b | 5.9 |
| 2c | 3.0 |

It was also assumed that the bladder would only stretch along its characteristic dimensions and that the maximum volume it could hold was 500 $cm^3$ (500 mL). Therefore, if it stretched along only one of its characteristic dimensions, the strain values (along the same direction) would be as shown in table 5.2. The same was done, firstly, considering that two of the three characteristic dimensions stretched (equally), table 5.3, and secondly, considering that all of them stretched (either equally), table 5.4.

Table 5.2: Deformation values when only one of the three characteristic values of the ellipsoid changes.

| **Unknown variable** | **New value (cm)** | **Deformation (%)** |
|---|---|---|
| a | 27 | 650 |
| b | 22 | 646 |
| c | 11 | 633 |

Table 5.3: Deformation values when two of the three characteristic values of the ellipsoid changes.

| **Unknown variables** | **New value (cm)** | **Deformation (%)** | **Direction** |
|---|---|---|---|
| a + b | 9.3 | 158 | a |
| a + b | 8.65 | 193 | b |
| a + c | 7.5 | 108 | a |
| a + c | 5.4 | 260 | c |
| b + c | 6.55 | 122 | b |
| b + c | 5.1 | 240 | c |

Table 5.4: Deformation values when all of the characteristic values of the ellipsoid changes.

| **Unknown variables** | **New value (cm)** | **Deformation (%)** | **Direction** |
|---|---|---|---|
| a + b + c | 5.92 | 64 | a |
| a + b + c | 5.27 | 79 | b |
| a + b + c | 3.82 | 155 | c |

Considering the results obtained in tables 5.2, 5.3 and 5.4 it is possible to realise that when it was considered that only one or two of the bladder characteristic dimensions stretch, strain values above 200% are obtained. This is obviously not realistic, since the bladder stretches along more directions that the ones considered and thus, such high values of strain won't be verified.

When it was considered that all its characteristic dimensions would stretch, the values of strain obtained were below 200%. Although this might induce to the conclusion that the bladder's wall is not subjected to strain values above 200% under normal conditions, it is important to bear in mind that the results obtained in table 5.4 are also not realistic. The bladder does not stretch equally in all directions.

Concerning that the studied cases are data from urodynamic tests, it is unlikely that strain values above 200% are obtained, since the maximum volume holded by patients is less than the 500 mL above considered. However, besides calibrating the bladder's wall behavior until 200% of strain, showed in figure 5.1, two more calibrations were made: one for the fibers alligned in a longitudinal direction and other for the fibers alligned in a circumferential direction, also showed in the same figure.

In order to calibrate the bladder's wall behavior, a test specimen model was created using Abaqus software, figure 5.3.

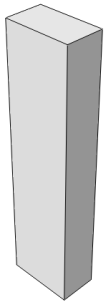

Figure 5.3: Test specimen created using Abaqus to calibrate the bladder's wall behavior with data from literature with 10cm×5.66cm×40cm.

Regarding the calibration of the bladder's wall behavior as a whole (values of strain until 200%), several constitutive models were used: the Neo-Hookean model, the Ogden model, the Yeoh model and the Martins model. For each of these constitutive models, two stress versus strain curves were obtained: the outcome of Abaqus simulation and the theoretical curve obtained with the parameters used within each model (without the contribution of the volumetric part). The latter was obtained using Excel. As far as Martins model is concerned, only the theoretical curve was obtained since the main purpose of using this model was to have a comparison between such a complex model (with the contribution of the muscle taken into account) and the most widely known constitutive models with respect to the difficulty in adjusting the curve of the models with the desired one. Hybrid hexahedral elements were used for every simulation.

Figure 5.4 shows the struggle the Neo-Hookean model had to mimic the bladder's wall behavior, revealing that it is not the appropriate model to be used. The theoretical curve and the simulation curve are overlapped.

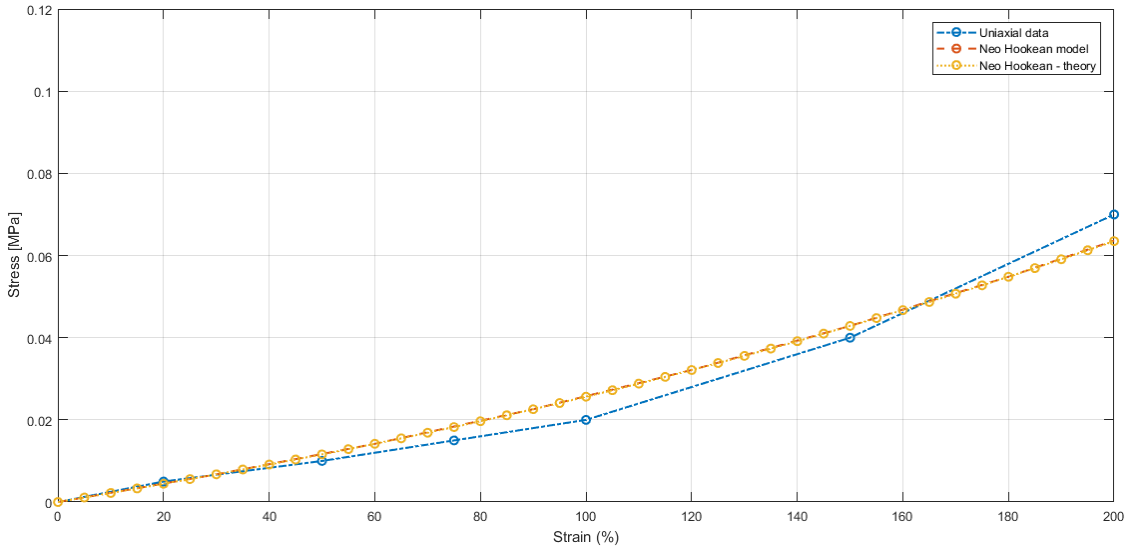


Figure 5.4: Mimicking bladder wall's behavior until 200% of deformation with Neo-Hookean model ($c_1 = 0.003664$ MPa; $D = 10^{-4}$ mm$^2$/N).

As regards the Ogden model, the simulation curve obtained was more satisfactory. It is shown in figure 5.5. In this case, a considerable difference was found between the theoretical curve and the simulation one. This difference might be due to the volumetric part contribution, which was not considered as already stated.

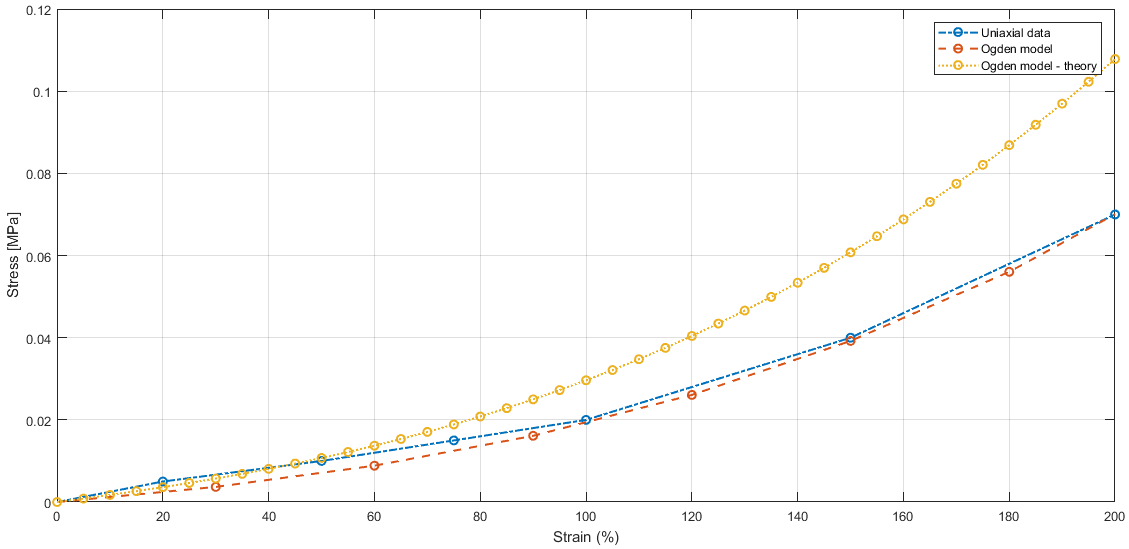


Figure 5.5: Mimicking bladder wall's behavior until 200% of deformation with Ogden model ($\mu_p = 0.0036$ MPa; $\alpha_p = 3.1$ MPa; $D = 10^{-4}$ mm$^2$/N; N = 1) .

Finally, the Yeoh and Martins models achieved curves were also very accurate and can be seen in figures 5.6 and 5.7, respectively.

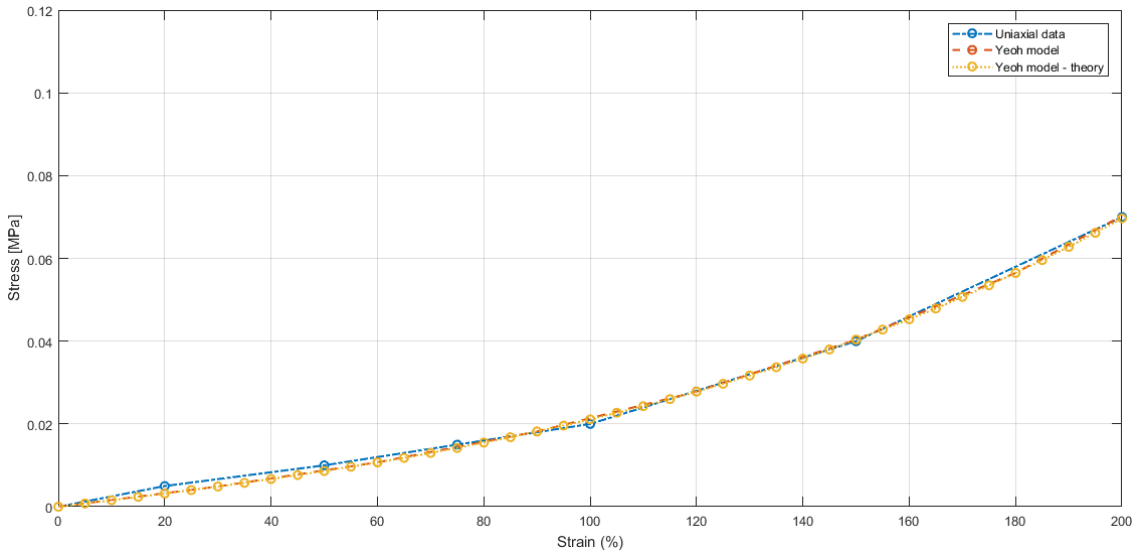


Figure 5.6: Mimicking bladder wall's behavior until 200% of deformation with Yeoh model ($c_1 = 0.00261$ MPa; $c_2 = 10^{-4}$ MPa; $c_3 = 5.90 \times 10^{-7}$ MPa; $D_1 = D_2 = D_3 = 10^{-4}$ mm$^2$/N).

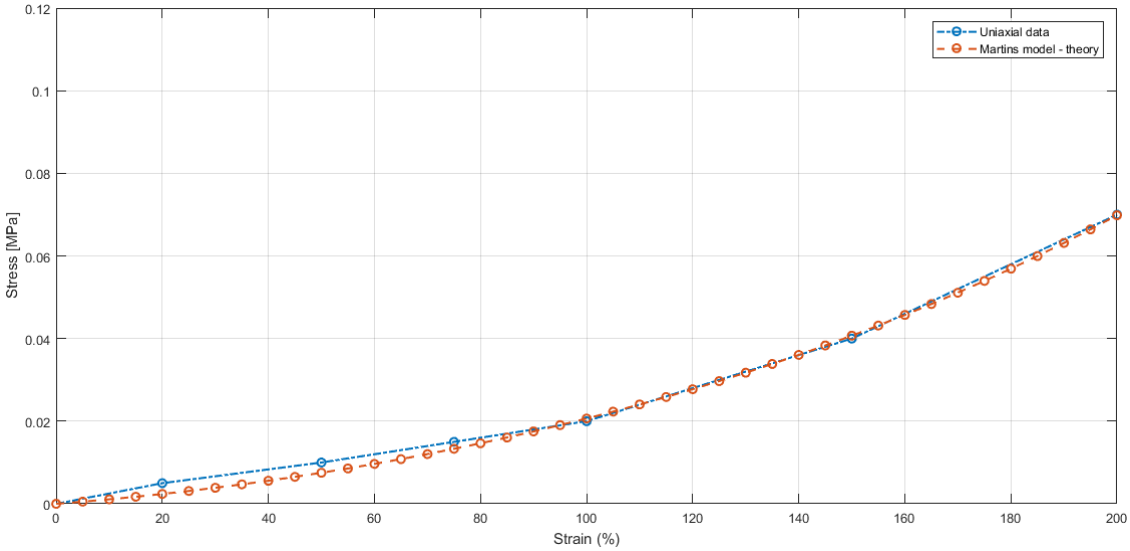


Figure 5.7: Mimicking bladder wall's behavior until 200% of deformation with Martins model ($c = 0.000000185$ MPa; $b = 0.1$; $A = 0.124$ MPa; $a = 0.04$; $D = 10^{-4}$ mm$^2$/N ).

In respect to the longitudinal and circumferential fibers' behavior, the Holzapfel-Gasser-Ogden model was used rather than the Neo-Hokean one. The outcome of these simulations are shown in figures 5.8 and 5.9.

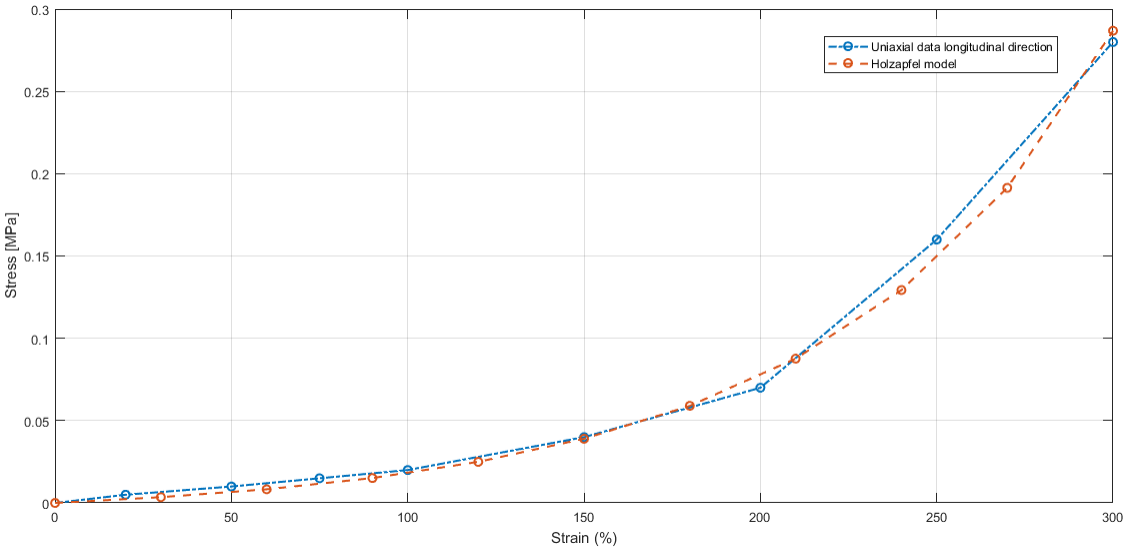


Figure 5.8: Mimicking the exterior and interior bladder wall layers' behavior (fibers alligned longitudinally) with Holzapfel-Gasser-Ogden model ($c_1 = 0.001719$ MPa; $k_1 = 0.0014949$; $k_2 = 0.010492$; $\kappa = 0.266$; $D = 10^{-4}$ mm$^2$/N ).

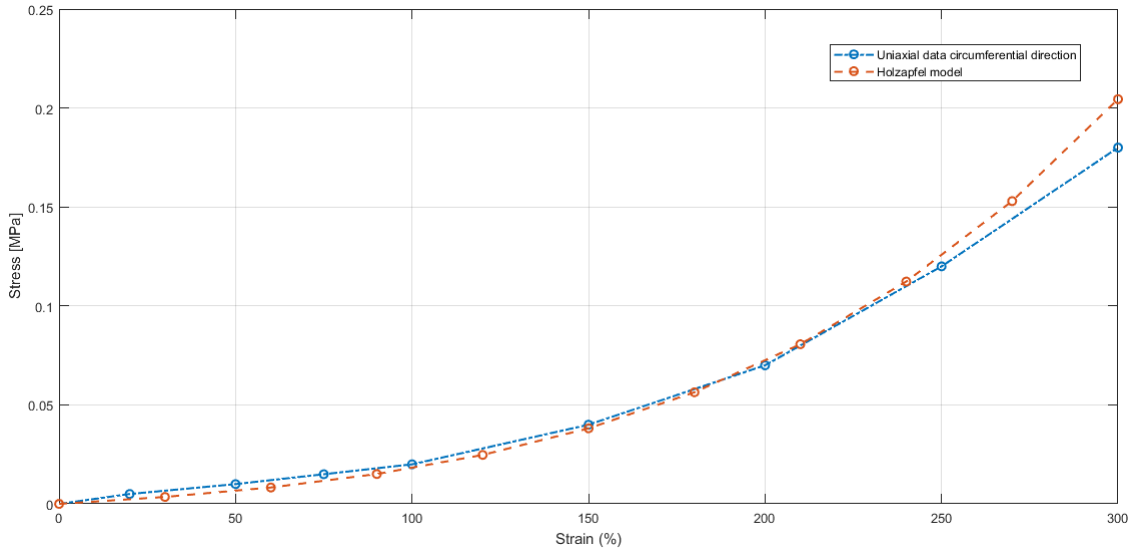


Figure 5.9: Mimicking the middle bladder wall layer's behavior (fibers alligned circumferentially) with Holzapfel-Gasser-Ogden model ($c_1 = 0.001719$ MPa; $k_1 = 0.0014949$; $k_2 = 5.246 \times 10^{-10}$; $\kappa = 0.266$; $D = 10^{-4}$ mm$^2$/N ).

The Holzapfel-Gasser-Ogden model revealed to be an interesting model to calibrate both longitudinal and circumferential fibers' behavior. The remaining models, as it was possible to realise by the results accomplished previously, can also be used to mimic these type of behaviors accurately.

In figures 5.10 and 5.11, as it was also observed in figure 5.5, a gap between the theoretical and the simulation curves can be seen, as regards to the Ogden constitutive model.

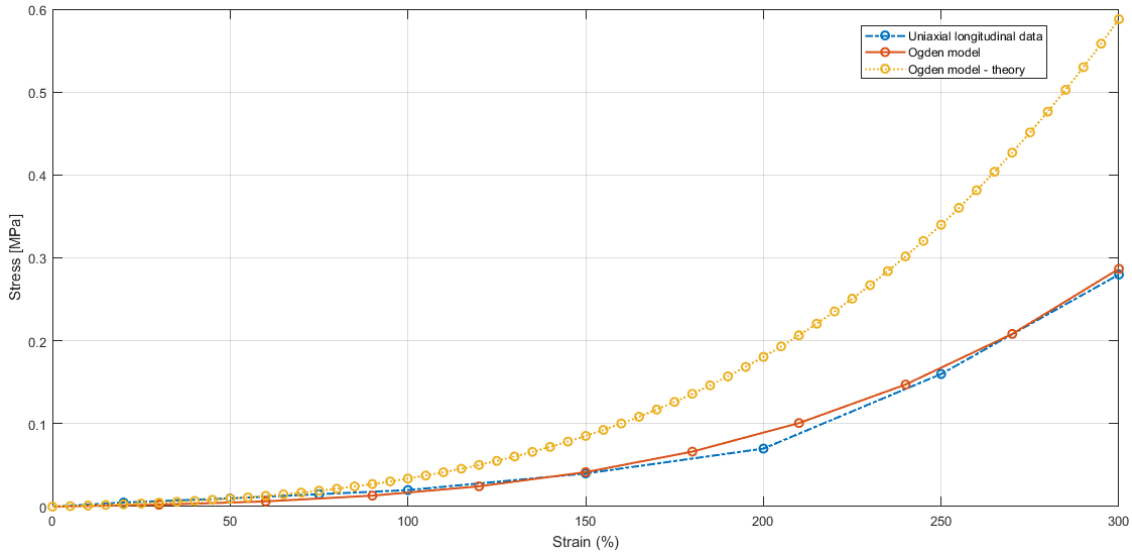


Figure 5.10: Mimicking the exterior and interior bladder wall layers' behavior (fibers alligned longitudinally) with Ogden model ($\mu_p = 0.002$ MPa; $\alpha_p = 4.1$ MPa; $D = 10^{-4}$ mm$^2$/N; $N = 1$).

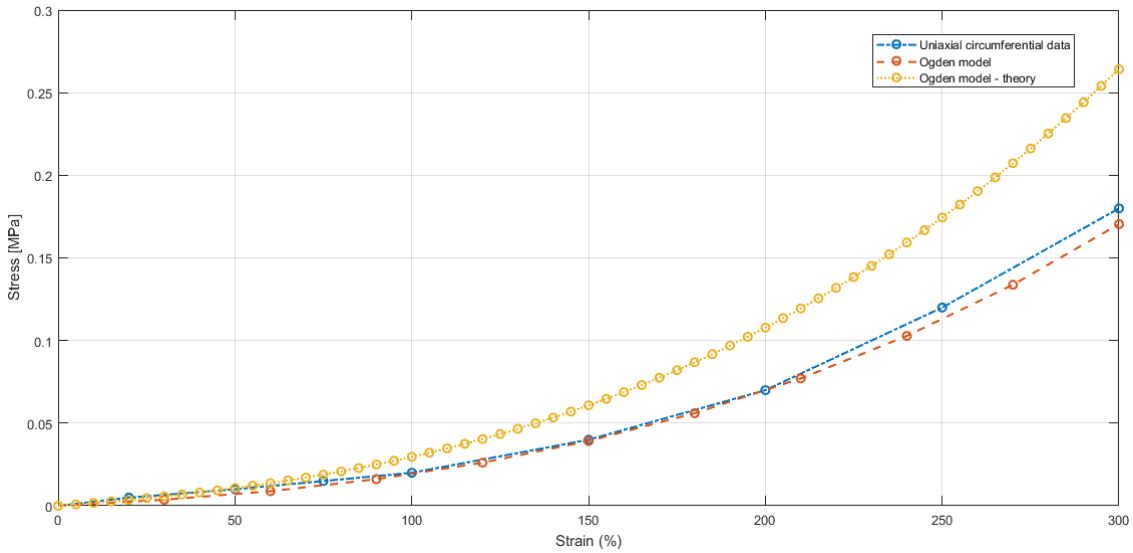


Figure 5.11: Mimicking the middle bladder wall layer's behavior (fibers alligned circumferentially) with Ogden model ($\mu_p = 0.0036$ MPa; $\alpha_p = 3.1$ MPa; $D = 10^{-4}$ mm$^2$/N; $N = 1$).

As far as the results obtained with the Yeoh and Martins models are concerned, these are shown in figures 5.12, 5.13, 5.14 and 5.15, respectively.

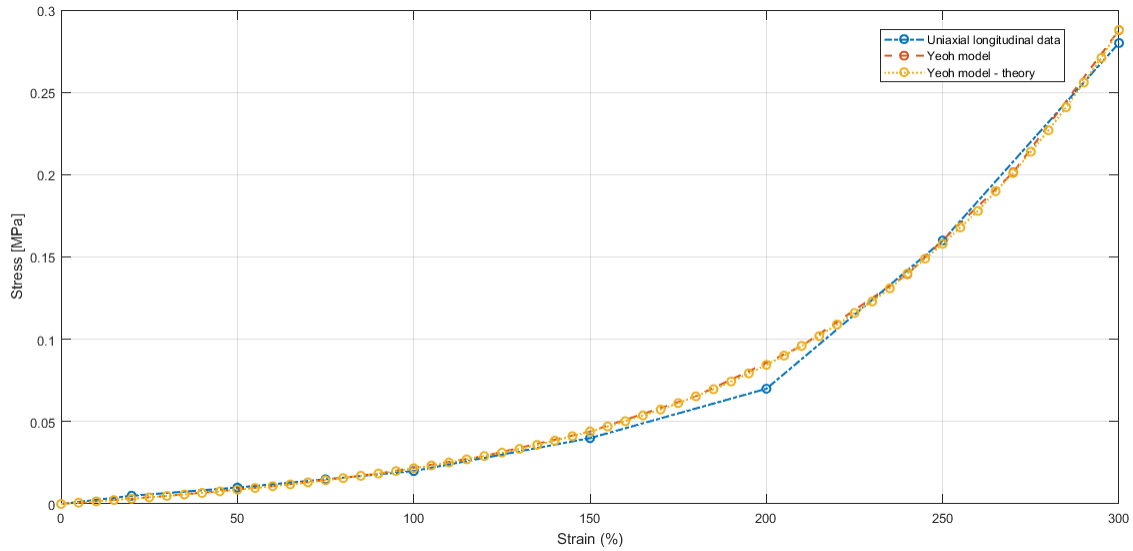


Figure 5.12: Mimicking the exterior and interior bladder wall layers' behavior (fibers alligned longitudinally) with Yeoh model ($c_1 = 0.00261$ MPa; $c_2 = 10^{-4}$ MPa; $c_3 = 7.0 \times 10^{-6}$ MPa; $D_1 = D_2 = D_3 = 10^{-4}$ mm$^2$/N).

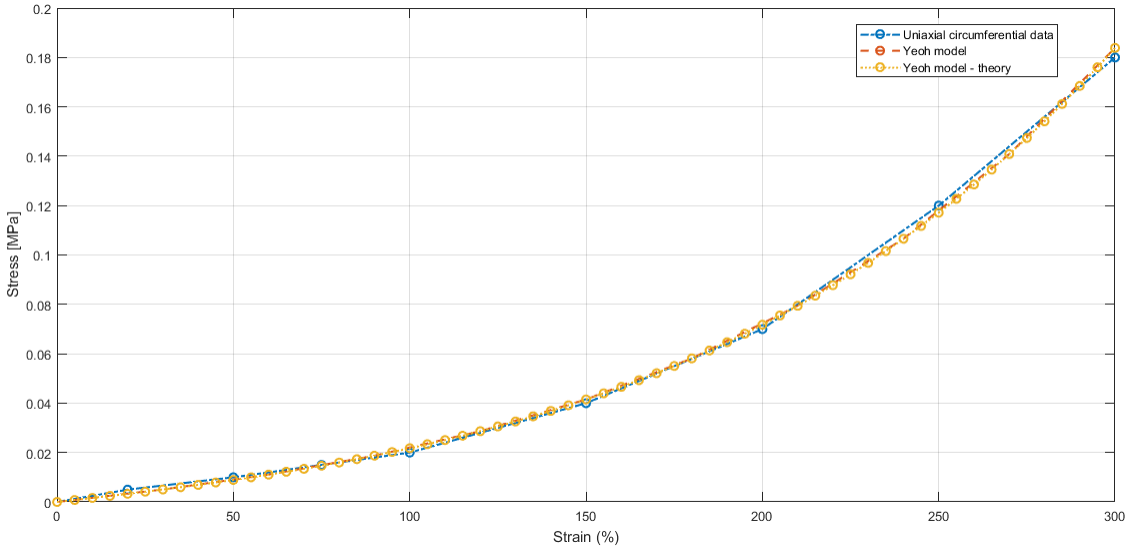


Figure 5.13: Mimicking the middle bladder wall layer's behavior (fibers alligned circumferentially) with Yeoh model ($c_1 = 0.0027$ MPa; $c_2 = 10^{-4}$ MPa; $c_3 = 8.0 \times 10^{-7}$ MPa; $D_1 = D_2 = D_3 = 10^{-4}$ mm$^2$/N ).

The Yeoh constitutive model adjusted almost perfectly to the porcine bladder's behavior disseminated by Jokandan, Ajalloueian et al., 2017 [27], proving to be one of the best models to mimic it.

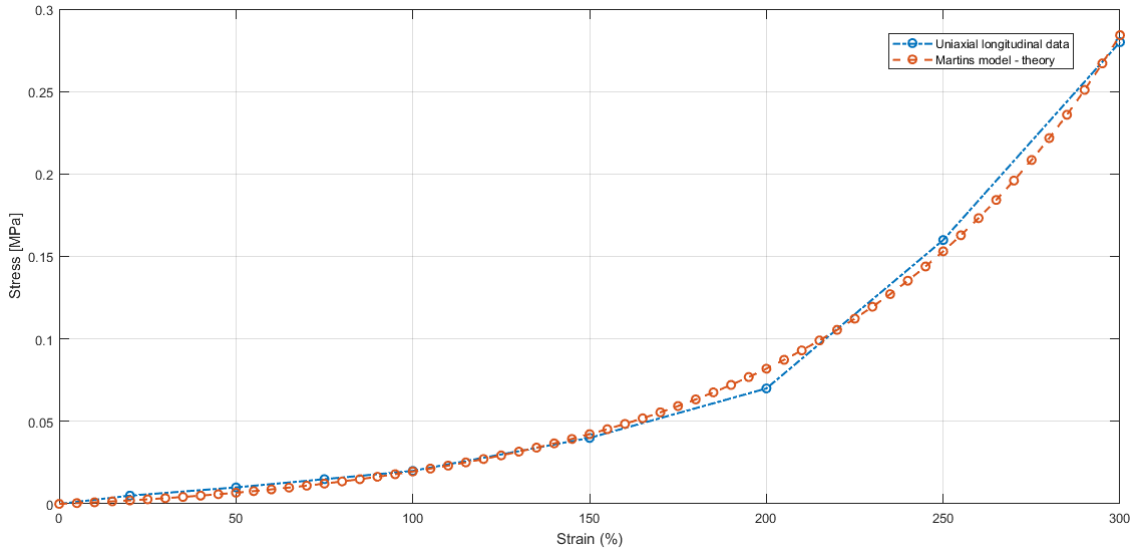


Figure 5.14: Mimicking the exterior and interior bladder wall layers' behavior (fibers alligned longitudinally) with Martins model ($c = 0.00000003$ MPa; $b = 0.2$; $A = 0.04$ MPa; $a = 0.11$; $D = 10^{-4}$ mm$^2$/N ).

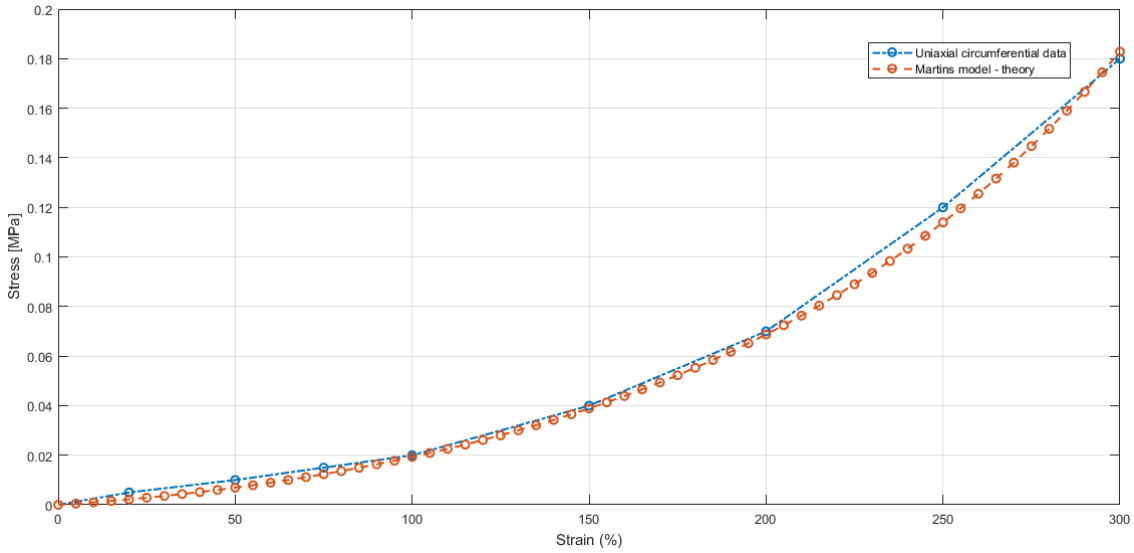


Figure 5.15: Mimicking the middle bladder wall layer's behavior (fibers alligned circumferentially) with Martins model ($c = 0.00000003$ MPa; $b = 0.3$; $A = 0.08$ MPa; $a = 0.057$; $D = 10^{-4}$ mm$^2$/N).

Before working on the existing 3D model of the bladder, in order to calibrate it with data from urodynamics, another mechanical test simulation was performed, named Ball Burst. This test was conducted by the same authors of the uniaxial tests that were used as a reference in the previous simulations.

The Ball Burst test consists in placing the opened bladder specimen on the circular aperture of a cylinder and to push forward a sphere through the aperture of it, perpendicularly. This test revealed to be a good one to obtain the mechanical properties of the bladder wall as a whole.

In figure 5.16 the 3D model used to mimic this test is shown and in figure 5.17 it is possible to observe the force versus displacement curve from the real test.

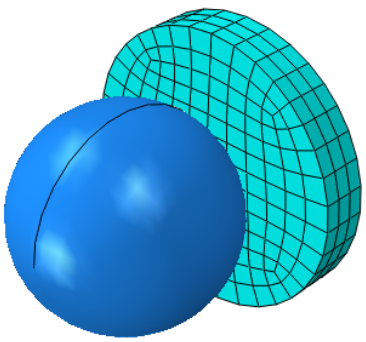

Figure 5.16: 3D BB test model created in Abaqus.

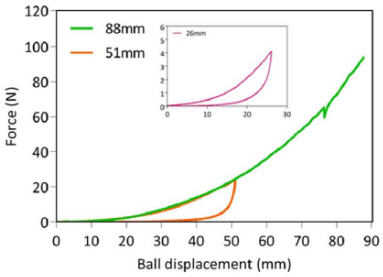


Figure 5.17: Force vs displacement outcome of BB test at different sphere displacements [27].

The Ogden, Yeoh and Holzapfel-Gasser-Ogden models were used in the Ball Burst simulations. Here, the simulations were carried out considering the fibers orientation - the bladder specimen used in the simulation was divided into three, mimicking the bladder's layers that have a crucial impact on its mechanical behavior. Thus, three simulations were carried out, one for each model used. For the outer and inner layers the corresponding constants for each model used, were those that best suited the corresponding data from the literature (showed previously). The same was done for the middle layer.

In every simulation performed it was not possible to mimic the whole curve (corresponding to 88 mm of displacement). The maximum value of displacement obtained was around 29 mm with the Holzapfel-Gasser-Ogden model. In each of them, hybrid hexahedral elements were used (since the geometry of the bladder specimen was not complex) and the mesh had 648 nodes and 429 elements. As far as boundary conditions are concerned, the posterior surface contour of the part mimicking the bladder tissue has the displacement allong its perpendicular direction constrained.

In figure 5.18 the force versus displacement curves obtained for each of the constitutive models used are illustrated, by comparison with the curve from the test performed by Jokandan, Ajalloueian et al., 2017 [27].

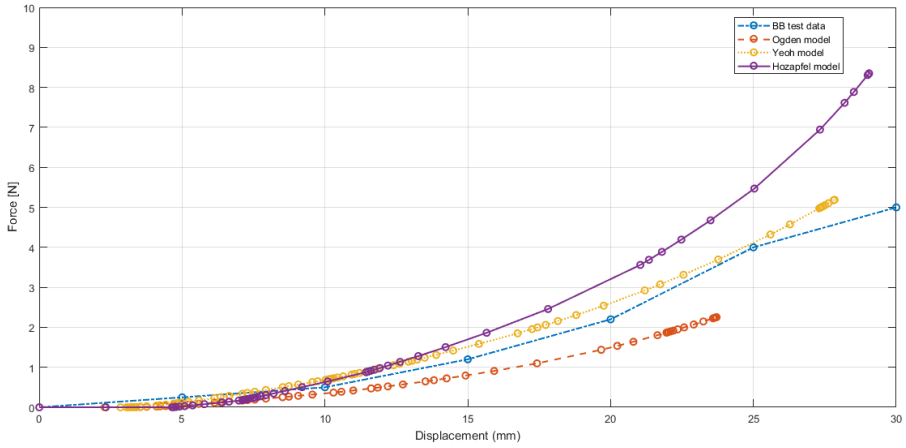


Figure 5.18: Force vs displacement outcome of BB test simulation with Ogden, Yeoh and Holzapfel-Gasser-Ogden models.

Until the values of displacement achieved in the simulations, the Yeoh model was the constitutive model that best mimicked the bladder's behavior in this test. Both Ogden and Holzapfel-Gasser-Ogden models mimicked competently the behavior illustrated in figure 5.17, initially. After 15 mm of displacement and until the maximum values obtained in each simulation, both curves slightly diverge from the reference curve.

In order to assess the impact of the mesh refinement a new simulation was carried out using the Yeoh model (since it was the one that best mimicked the bladder's behavior in this test). In the new mesh, illustrated in figure 5.19, the number of nodes were raised to 8526 and the number of elements to 6972.

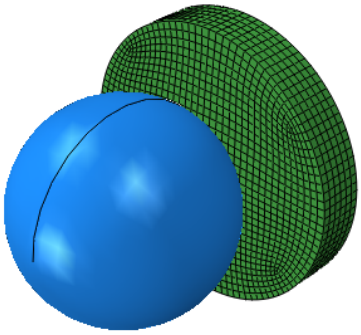

Figure 5.19: 3D BB test model with the mesh refined.

In figure 5.20 the comparison between the first mesh and the refined one is shown.

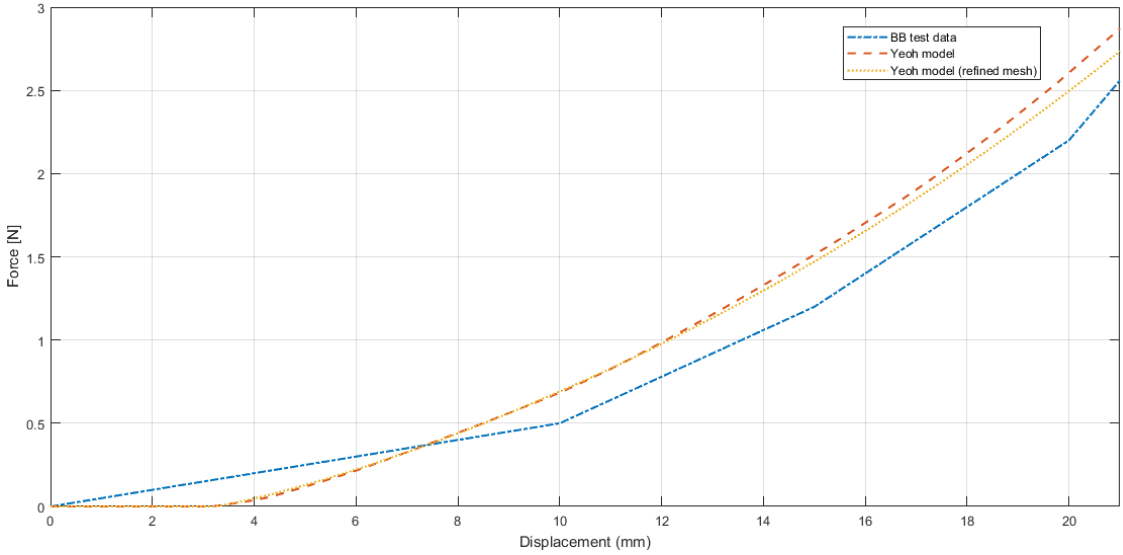


Figure 5.20: Influence of the mesh refinement.

As it is possible to see, although the curve refering to the mesh refinement moved closer to the reference one, it did not have a big impact on the outcome, at least until the values of displacement

that were possible to obtain in these simulations.

Another attempt was carried out introducing incompatible modes, as it would help improving the outcome regarding the type of problem that is being analysed. The results can be seen in figure 5.21. In this case, the refined mesh was not used.

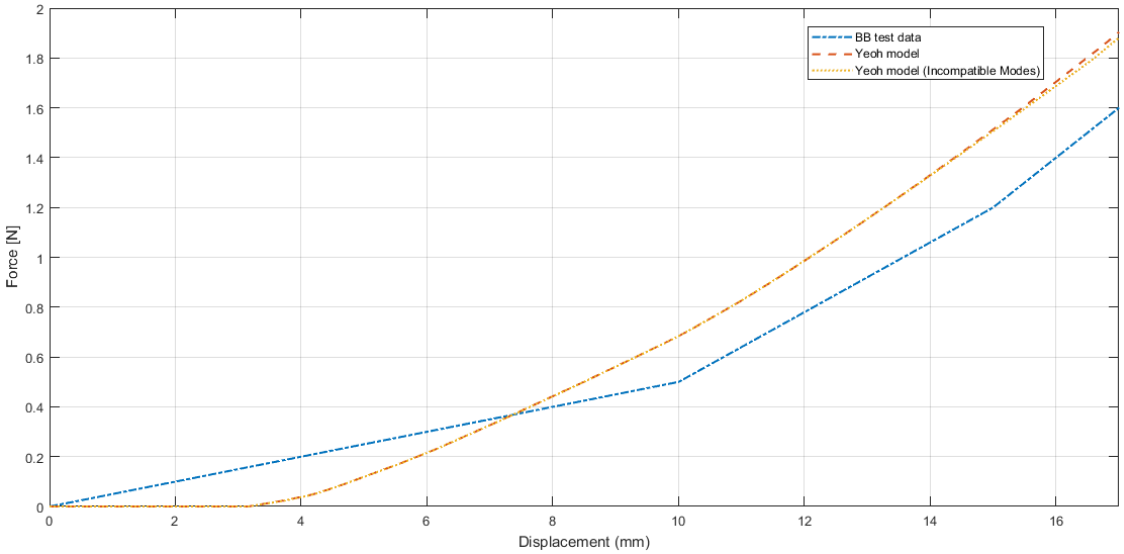


Figure 5.21: Influence of the introduction of incompatible modes.

The introduction of incompatible modes did not have the expected effect, since both curves are overlapped and thus, there were no significant changes observed.

Finally, regarding the bladder's simulations, the main goal was to understand the material mechanical changes existing between a bladder associated with no urinary incontinence and a bladder with different types of urinary incontinence.

The Yeoh constitutive model was the model chosen to characterize the bladder's wall mechanical behavior in the following simulations. The 3D geometrical model (comprising the bladder, the urethra and the pubis of a nulliparous 24-years female without pelvic floor dysfunction complaints) used hereafter is shown in figure 5.22. Hybrid hexahedral elements were used on the part related to the bladder and hybrid tetrahedral elements were used on the part related to the pubis. The part mimicking the bladder has 6724 nodes and 5016 elements, while the pubis' model has 3171 nodes and 13054 elements. In terms of boundary conditions, the urethra's inferior surface was fixed and it was also established surface-to-surface contact between part of the bladder's surface that is located near the pubis and the corresponding surface of the latter.

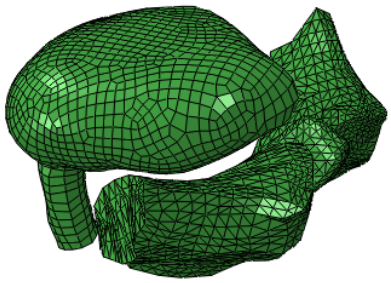

Figure 5.22: 3D geometrical model of the bladder and pubis.

In terms of the simulations that were conducted, the part related to the pubis in this model had no influence on the results whatsoever. Its influence, concerning the contact that might happen in a real situation and its influence on the final outcome, was not the aim of these simulations. Its presence in the model is related to the fact that it, in conjunction with the bladder, was obtained based on magnetic resonance imaging (MRI) and it is usually used as reference as far as displacement and rotation of the bladder and urethra are concerned.

The first simulation concerning this model was carried out using the parameters of the Yeoh model that were used to calibrate the bladder's behavior as a whole, figure 5.6. A curve relating pressure (relative pressure) and volume inside the bladder were obtained, showing the normal pressure versus volume relation in the storage phase (until 400 mL, since it was the maximum volume the person submited to these urodynamic tests could storage, as it can be seen forward), figure 5.23.

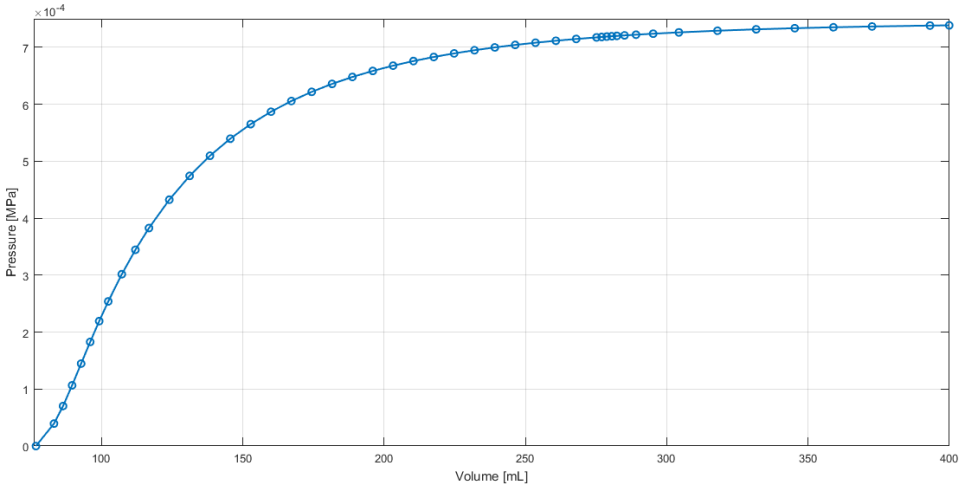


Figure 5.23: Relation between pressure and volume inside the bladder in the storage phase until 400 mL.

The second simulation embraces the calibration of the same geometrical model with data from an ALPP (inducing the existence of stress urinary incontinence), illustrated in figure 5.24. In this case, the two points of this figure used are marked on it in red. Only these two points were

used, firstly, because there are few points available in the test and, secondly, because with the constitutive model used it is not possible to achieve a curve fluctuating around values of 30 $cmH_2O$ and 50 $cmH_2O$, that are the values observed in this case.

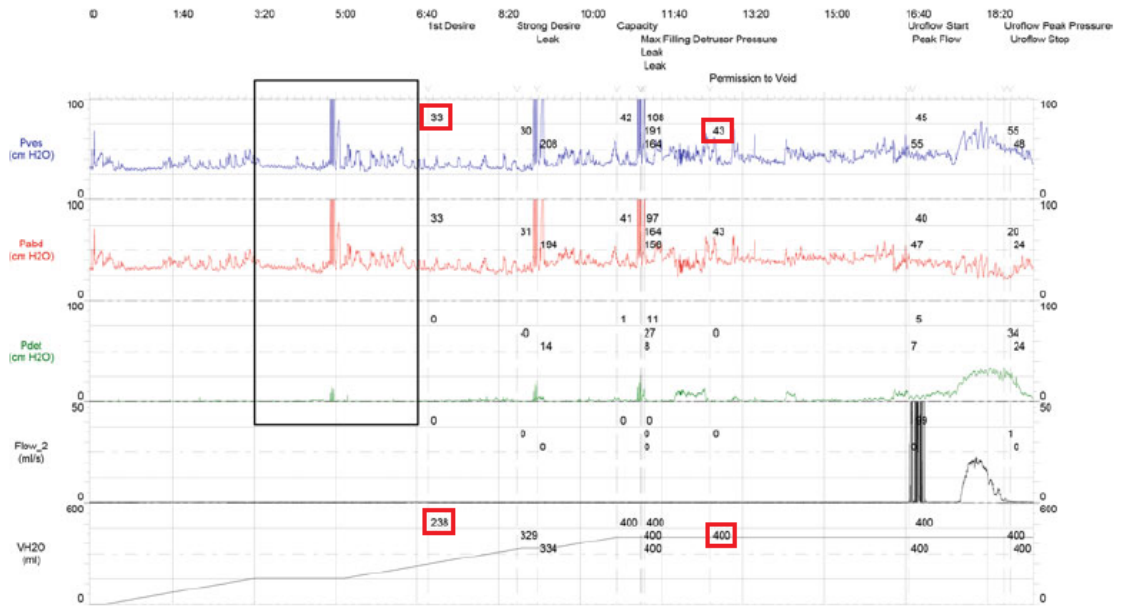


Figure 5.24: Abdominal leap point pressure - multichannel cystometry showing leak point pressure [16].

The shape of the curve, relating the pressure and volume inside the bladder, related to this simulation, is shown in figure 5.25, along with the curve already shown in figure 5.23.

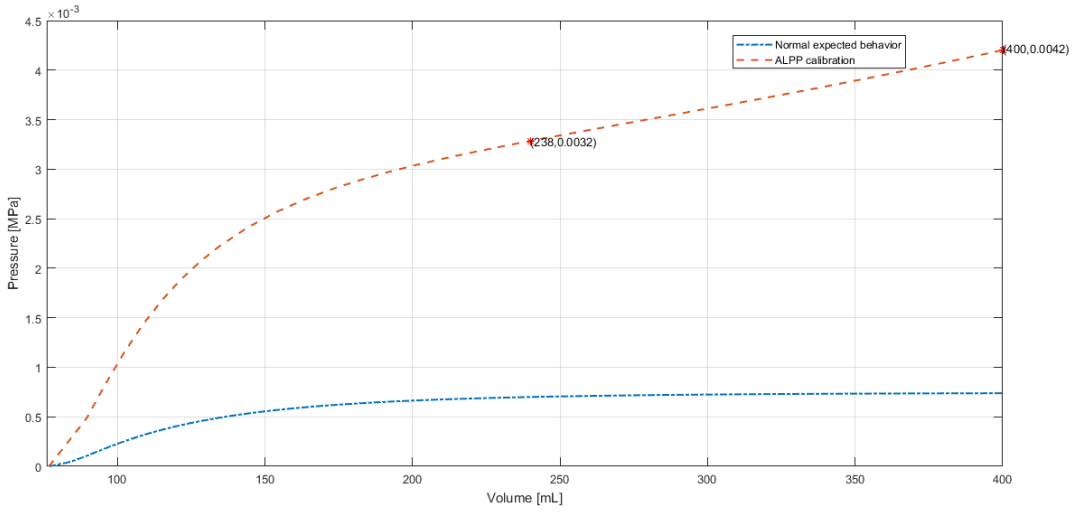


Figure 5.25: Comparison between the expected pressure versus volume curve and the homologous corresponding to a stress urinary incontinence situation.

The obtained curve reached the two desired points, as it can be seen in figure 5.25. The parameters used in the Yeoh model were: $c_1 = 0.0119\ MPa$; $c_2 = 10^{-4}\ MPa$; $c_3 = 3.25 \times 10^{-4}\ MPa$; $D_1 = D_2 = D_3 = 10^{-4}\ mm^2/N$. It is clearly seen that the bladder's wall in a situation where stress urinary incontinence occurs is stiffer than in a normal one, since for the same value of volume inside it the pressure is higher and, as a result, it is less compliant.

It is also interesting to compare the curves relating stress and strain that characterize the bladder's wall material behavior. In figure 5.26 is illustrated the curves for both cases. These are the originating theoretical curves (without the volumetric part accounted) regarding the parameters used for both.

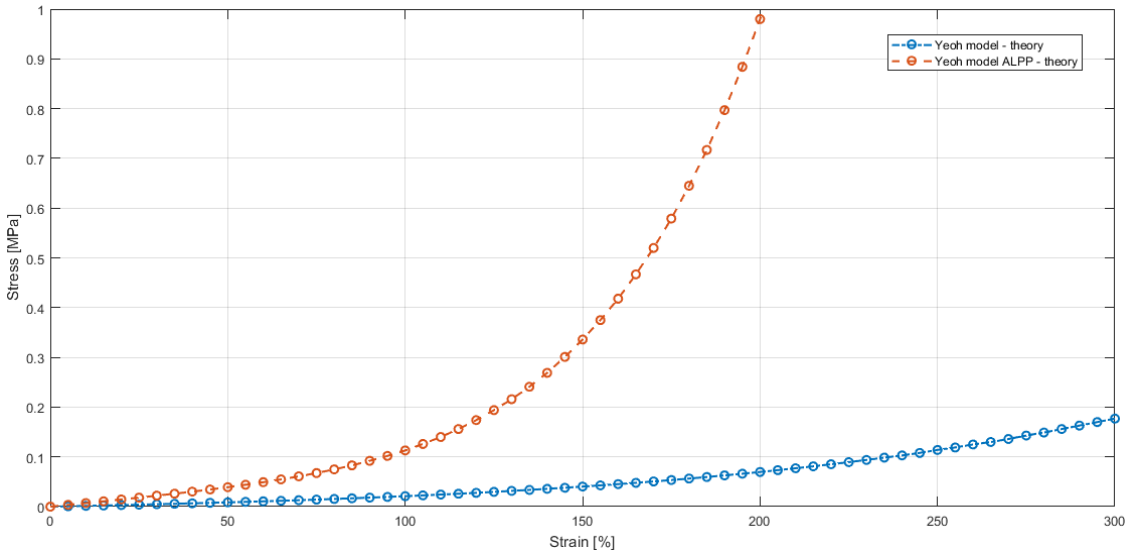


Figure 5.26: Comparison between a normal stress versus strain curve, for the bladder's material behavior, and the homologous corresponding to a stress urinary incontinence situation.

Although the bladder's wall material behavior might not be exactly how the curve illustrated above looks like (since only two points were used to calibrate it), as well as the pressure versus volume curve related to the ALPP situation, it is certainly placed above the other curve, meaning that a higher stress is required to produce the same value of strain, and thus, the material of the bladder's wall is stiffer in this case.

As far as the following simulation is concerned, a situation of an overactive bladder was considered, figure 5.27. As regards to this case, two points were also used to access the difference in behavior of the bladder's wall in all of the three cases.

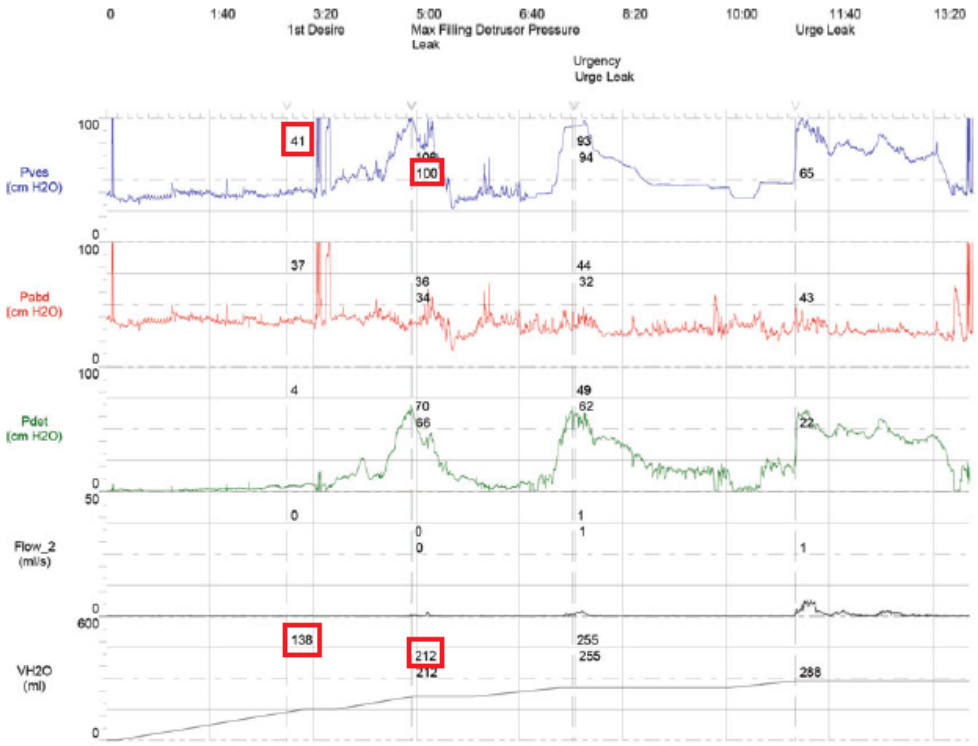


Figure 5.27: Detrusor overactivity - multichannel cystometry showing detrusor overactivity [16].

In figure 5.28 is shown the comparison of the pressure versus volume inside the bladder between the three cases. Once more, the resulting curve for this last situation is shown, despite only the points used being meaningful, since muscle activity is also observed and was not considered. The relevance of the curves is due to their identification, as well as for the meaningful points.

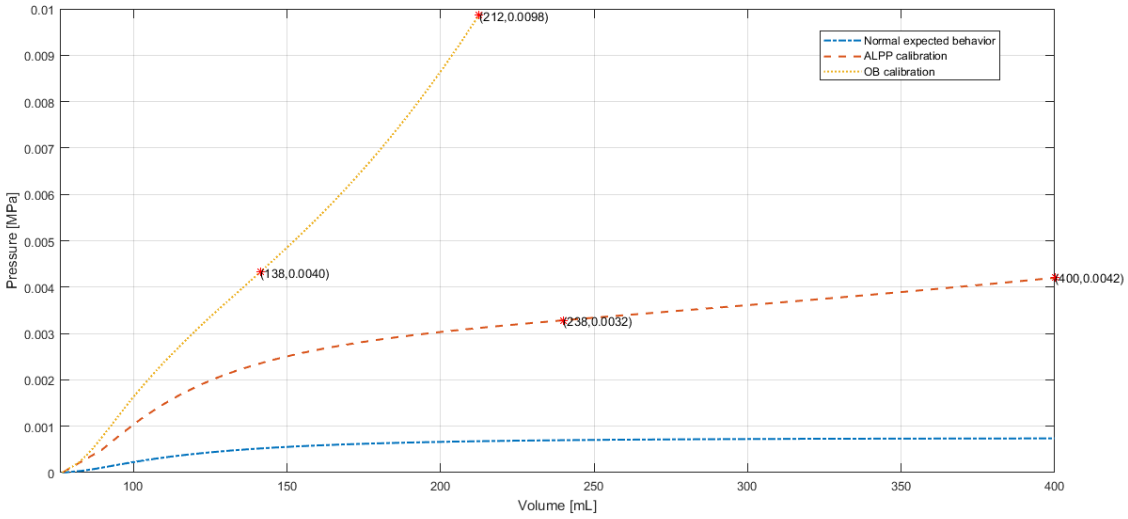


Figure 5.28: Comparison between the expected pressure versus volume curve and the homologous corresponding to a stress urinary incontinence situation and an overactive bladder.

The parameters used in the Yeoh model for the overactive bladder case were: $c_1 = 0.0185\ MPa$; $c_2 = 0.0035\ MPa$; $c_3 = 0.0091\ MPa$; $D_1 = D_2 = D_3 = 10^{-4}\ mm^2/N$. In this last case, the bladder is even less compliant than in the previous one, showing that the bladder's wall here is even stiffer.

# Chapter 6

# Conclusion and Future Work

## 6.1 Conclusion

The bladder's wall behavior was mimicked by reproducing experimental tests from the literature using different constitutive models. Thereafter, the calibration of the bladder and urethra model was performed according to data provided by urodynamics.

As far as the different constitutive models used to mimic the bladder's wall behavior are concerned, the Neo-Hookean model showed not to be the appropriate model to mimic this type of behavior. The other models used (Ogden, Yeoh, Martins and Holzapfel-Gasser-Ogden), revealed to be highly accurate, representing the desired behavior (both longitudinal and circumferential fibers behavior) successfully. The Yeoh model exhibited the most precise behavior.

Regarding the Ball Burst simulation, an obstacle was found - the entire forces versus displacement curve was not achieved due to the excessive bending verified. Until the maximum displacement reached, the Yeoh model showed to be the best model to resemble the bladder's wall behavior. Mesh refinement improved slightly the result obtained with this model by making the simulation curve closer to the experimental one. The introduction of incompatible modes did not improve the outcome as it was predicted, regarding the type of problem reproduced.

Finally, the simulations performed with the bladder and urethral model showed that in both cases, stress urinary incontinence and overactive bladder, the bladder's wall is stiffer and thus, less compliant, in spite of not being able to use many points to calibrate the model with the urodynamic data. They also allowed to realise that a more complex constitutive model should be used so as to mimic the muscle contractions and therefore, being able to calibrate the model rigorously. Afterwards, these models could be used to mimic surgical procedures used to rectify the type of urinary incontinence in study.

## 6.2 Future Work

In terms of future work, it would be important to compare the results obtained, regarding the bladder's wall behavior, with the behavior of horse's bladder, since it is believed to have a closer

behavior to human's bladder than procine's bladder.

A more complex constitutive model, for example the Martins model, should also be used in order to have a better representation of the bladder's behavior when stress urinary incontinence and/or overactive bladder are present. It cam simulate detrusor contractions, therefore it is possible to achieve more realistc results when calibrating data derived from urodynamics. It would also be interesting, to use the same model, to mimic more examples of the same urinary incontinece, so as to check if there is any pattern associated in terms of mechanical properties and mechanical changes.

It would also help in terms of applying more realistic boundary conditions and interactions, to add the bladder's surrounding organs.

# References


[1] J.A.C. Martins, E.B. Pires, R. Salvado, and P.B. Dinis. A numerical model of passive and active behavior of skeletal muscles. *Computer Methods in Applied Mechanics and Engineering*, 151(3):419 – 433, 1998. Containing papers presented at the Symposium on Advances in Computational Mechanics.

[2] D. R. Hickling, Tung-Tien Sun, and Xue-Ru Wu. Anatomy and physiology of the urinary tract: relation to host defense and microbial infection. *Microbiology Spectrum*, 3(4), 2015.

[3] A. K. Patel and C. R. Chapple. Anatomy of the lower urinary tract. *Surgery (Oxford)*, 26(4):127 – 132, 2008. Renal and urology I.

[4] InnerBody, May 2018. URL: http://www.innerbody.com/image/urinov.html.

[5] Virtual Medical Centre, May 2018. URL: https://www.myvmc.com/anatomy/urinary-tract/.

[6] Russell H. and Williams M.D. Anatomy & function of the urinary tract. 2015.

[7] A.N. Natali, A.L. Audenino, W. Artibani, C.G. Fontanella, E.L. Carniel, and E.M. Zanetti. Bladder tissue biomechanical behavior: experimental tests and constitutive formulation. *Journal of Biomechanics*, 48(12):3088 – 3096, 2015.

[8] F. Ajalloueian, G. Lemon, J. Hilborn, I. Chronakis, and M. Fossum. Bladder biomechanics and the use of scaffolds for regenerative medicine in the urinary bladder. 15, 02 2018.

[9] J. Jung, H. K. Ahn, and Y. Huh. Clinical and functional anatomy of the urethral sphincter. *International Neurourology Journal*, 16(3):102, 2012.

[10] V. Monteiro, E. Oñate, and S. Oller. *Computational model of the human urinary blader*. Centre Internacional de Mètodes Numèrics en Enginyeria (CIMNE), 2013.

[11] Paul Abrams, Linda Cardozo, Saad Khoury, and Alan Wein. *Incontinence*. European Association of Urology, fifth edition edition, 2013.

[12] International Continence Society, May 2018. URL: https://www.ics.org/terminology/19.

[13] Urology Care Foundation, May 2018. URL: https://www.urologyhealth.org/urologic-conditions/urinary-incontinence.

[14] The Canadian Continence Foundation, May 2018. URL: http://www.canadiancontinence.ca/EN/what-is-urinary-incontinence.php.

[15] Roustem N. Miftahof and Hong Gil Nam. *Biomechanics of the Human Urinary Bladder*. Springer-Verlag Berlin Heidelberg, first edition, 2013.

[16] N.Kow and M. F. R. Paraiso. Urodynamic testing. *Springer Science+Business Media New York*, pages 149–161, 2015.

[17] Y. Zhang, S. Kim, A. G. Erdman, K. P. Roberts, and G. W. Timm. Feasibility of using a computer modeling approach to study SUI induced by landing a jump. *Annals of Biomedical Engineering*, 37(7):1425–1433, may 2009.

[18] Eduardo W. Chaves. *Notes on Continuum Mechanics*, volume 4. Springer Netherlands, first edition, 03 2013.

[19] Abaqus, May 2018. URL: http://abaqus.software.polimi.it/v6.14/books/stm/default.htm?startat=ch04s06ath125.html.

[20] P. A. L. S. Martins, R. M. Natal, and A. J. M. Ferreira. A comparative study of several material models for prediction of hyperelastic properties: application to silicone-rubber and soft tissues. *Strain*, 42(3):135–147. arXiv:https://onlinelibrary.wiley.com/doi/pdf/10.1111/j.1475-1305.2006.00257.x.

[21] M.P.L. Parente, R.M. Natal Jorge, T. Mascarenhas, A.A. Fernandes, and J.A.C. Martins. The influence of the material properties on the biomechanical behavior of the pelvic floor muscles during vaginal delivery. *Journal of Biomechanics*, 42(9):1301 – 1306, 2009.

[22] R. Lakes and F. Kulacki. *Viscoelastic Solids*. CRC Press, 1998.

[23] David Roylance. Engineering viscoelasticity, 2001.

[24] Nihat Özkaya, Dawn Leger, David Goldsheyder, and Margareta Nordin. *Mechanical Properties of Biological Tissues*, pages 361–387. Springer International Publishing, Cham, 2017.

[25] J. N. Reddy. *Introduction to the Finite Element Method*. McGraw-Hill Education, third edition, 2006.

[26] Eugenio Oñate. *Structural Analysis with the Finite Element Method - Linear Statics*, volume 1. Springer, 2013.

[27] M. S. Jokandan, F. Ajalloueian, M. Edinger, P. R. Stubbe, S. Baldursdottir, and I. S. Chronakis. Bladder wall biomechanics: a comprehensive study on fresh porcine urinary bladder. *Journal of the Mechanical Behavior of Biomedical Materials*, 79:92–103, mar 2018.